Summer 2022

SYNTHETIC GECKO INSPIRED DRY ADHESIVE THROUGH TWO-PHOTON POLYMERIZATION FOR SPACE APPLICATIONS

Zefu Ren
renz@my.erau.edu

Scholarly Commons Citation

Ren, Zefu, "SYNTHETIC GECKO INSPIRED DRY ADHESIVE THROUGH TWO- PHOTON POLYMERIZATION FOR SPACE APPLICATIONS" (2022). *PhD Dissertations and Master's Theses*. 671.
https://commons.erau.edu/edt/671

SYNTHETIC GECKO INSPIRED DRY ADHESIVE THROUGH TWO- PHOTON POLYMERIZATION FOR SPACE APPLICATIONS

By

Zefu Ren

A Thesis Submitted to the Faculty of Embry-Riddle Aeronautical University
In Partial Fulfillment of the Requirements for the Degree of
Master of Science in Aerospace Engineering

August 2022
Embry-Riddle Aeronautical University
Daytona Beach, Florida

SYNTHETIC GECKO INSPIRED DRY ADHESIVE THROUGH TWO- PHOTON POLYMERIZATION FOR SPACE APPLICATIONS

By

Zefu Ren

This Thesis was prepared under the direction of the candidate's Thesis Committee Chair, Dr. Daewon Kim, Department of Aerospace Engineering, and Co-Chair, Dr. Foram Madiyar, Department of Physical Science, and has been approved by the members of the Thesis Committee. It was submitted to the Office of the Senior Vice President for Academic Affairs and Provost, and was accepted in the partial fulfillment of the requirements for the Degree of Master of Science in Aerospace Engineering.

THESIS COMMITTEE

Chair, Dr. Daewon Kim	Co-Chair, Dr. Foram Madiyar
Member, Dr. Mandar Kulkarni	
Graduate Program Coordinator, Dr. Hever Moncayo	Date
Dean of the College of Engineering, Dr. James W. Gregory	Date
Associate Provost of Academic Support, Dr. Christopher Grant	Date

ACKNOWLEDGEMENTS

Foremost, I would like to express my tremendous appreciation to my advisor, Dr. Daewon Kim, who was consistently patient while providing invaluable suggestions and encouragement throughout my master's journey. His guidance and counseling motivated me to accomplish my thesis. I also would like to thank Dr. Foram Madiyar for providing access to the chemistry lab and serving as the co-chair of my committee. Additionally, I would like to thank Dr. Mandar Kulkarni for joining my thesis committee and providing his valuable suggestions on my thesis. Mr. William Russo has also helped me building various tools for the experiments.

I want to thank Dr. Stanislav Sikulskyi for his advice on experiment setup improvement. I am also grateful to Taylor Stark and Rishikesh Srinivasaraghavan Govindarajan for helping me print tested samples and take SEM for my samples, respectively. I am also thankful for many helps from Danayit T. Mekonnen, Giovanna Curi Canonico Chioro, Katelyn D. Branaman and Scott Bender in guiding me to overcome the challenge of foreign language writing.

Lastly, my thanks would go to my beloved family for their loving consideration and financial support. They raised me to become an adult that can keep moving forward regardless of the situation. Meanwhile, I want to thank my girlfriend, who accompanied me to finish my master's degree and brought me spiritual encouragement.

This thesis material is based upon work supported in part by the National Science Foundation under Grant No. 2018853. The opinions, findings, and conclusions, or recommendations expressed are those of the author and do not necessarily reflect the views of the National Science Foundation.

ABSTRACT

This work aims to develop an advanced and cost-effective fabrication process to produce a simplified gecko-inspired microstructure with two-photon polymerization and polymer molding, aimed to improve the adhesive properties of microstructures. Such adhesive microstructures can be implemented for multi-purpose adhesive grasping devices, which have recently gained significant interest in the space exploration sector. Previous gecko-inspired microstructures were reviewed, and the new gecko-inspired microstructures have been developed with the adaptation of additive manufacturing methods for facile fabrication. The examined microstructures in this thesis were the tilted mushroom-shaped and wedge-shaped designs, which could both maximize adhesion by shearing the micropillars toward the tilted direction when preload force is applied. The improved microstructure fabrication process could produce micropillars in the height of 270 µm with soft polymer without defects. However, the miniaturized micropillars in the height of 40 µm, frabricated with the same process, had broken tips and missing structures. The effects of the scale, height, and shape of the micropillars in controllable dry adhesion were investigated through the experiments. The adhesion of the microstructures with artificial gecko setae in the height of 270 µm was 2 times higher than the microstructures with 40 µm of height.

Meanwhile, the microstructures that consisted of long and short artificial gecko setae had inferior adhesive performance to the microstructures having uniform long setae on all tested surfaces. Meanwhile, the result showed no direct correlation between the surface roughness of the attached surface and the adhesive performance of the microstructures. The wedge-shaped design was determined to have higher adhesion than the tilted mushroom-shaped design due to lower structural resistance on bending and higher effective contact area.

TABLE OF CONTENTS

ACKNOWLEDGEMENTS i

ABSTRACT ii

TABLE OF CONTENTS iii

LIST OF FIGURES vi

LIST OF TABLES ix

NOMENCLATURE x

1 Introduction 1

- 1.1 Gecko-inspired Dry Adhesion for Space Debris Removal 1
- 1.2 Gecko-inspired Dry Adhesion Microstructure 3
  - 1.2.1 Non-tilted artificial seta 4
  - 1.2.2 Tilted artificial seta 6
- 1.3 Design Parameters 8
  - 1.3.1 Material 8
  - 1.3.2 Tilted angle 9
  - 1.3.3 Sizes, Aspect Ratio, and Spacing 9
- 1.4 Fabrication Process 10
- 1.5 Motivations 11
- 1.6 Objectives 11

2 Microstructures Fabrication Process 13

- 2.1 Microstructure Design 13
- 2.2 Printing Microstructure Master Mold 15

2.3 Surface Treatment 17
2.3.1 Gold Sputtering 18
2.3.2 Micropipette Liquid Deposition 18
2.3.3 Spin Coating 19
2.4 Fabrication of Negative Molds and Positive Molds 20
2.4.1 No Surface Treatment 21
2.4.2 Gold Sputtering 23
2.4.3 Micropipette Liquid Deposition 23
2.4.4 Spin Coating 25
2.4.5 Replicated Positive Mold 26
2.5 Finalized Fabrication Procedure 28
3 Performance of Dry Adhesion 32
3.1 Tested Microstructures Designs 32
3.2 Roughness of Tested Surface 35
3.3 Equipment Setup 36
3.4 Result and Analysis 39
3.4.1 Effect of PAA Isolated Layer 40
3.4.2 Adhesion of Pure PDMS Flat Plane on Various Surfaces 42
3.4.3 Adhesion Comparison for Unifrom Height and Alternating Height Design ... 43
3.4.4 Adhesion Comparison for Scale Difference and Shape Difference 46

3.4.5 Numerical analysis 52

4 Conclusion.. 58

5 Future Work 60

REFERENCE... 61

LIST OF FIGURES

Figure 1.1 (a) Gecko’s foot and (b) detail view of its toe. 3

Figure 1.2 Example of active mode and release mode of the wedge-shaped artificial seta designs. 4

Figure 1.3 Example of the non-tilted cylinder-shaped and mushroom-shaped artificial seta designs. 5

Figure 1.4 Example of tilted microstructure designs. (a) Tilted cylinder-shape design. (b) Tilted mushroom-shape design. (c) Wedge-shaped design. 7

Figure 2.1 CATIA model of multi-design structure panel. (a) Step-structure design. (b) two-wall design. (c) Thick plane rectangular standard shape. (d) Sample of artificial gecko seta design. 14

Figure 2.2 The drawing of individual structures in multi-design structure panel with dimensions. (a) Thick plane rectangular standard shape. (b) Step-structure design. (c) Two-wall design. (d) Sample of artificial gecko seta design. 14

Figure 2.3 Tilted mushroom-shaped design from Busche *et al.* [30]. (a) Front view. (b) Side view (unit: µm). (c) Isometric view in CATIA. 15

Figure 2.4 Printed master molds on silicon wafer. (a) Top view of multi-design structure panel array. (b) Angled view of artificial gecko setae array. 17

Figure 2.5 Multi-design structure panel treated with gold sputtering 18

Figure 2.6 Multi-design structure panel treated with 5 microliters of (a) 5% Polyacrylic acid and (b) PEDOT: PSS 19

Figure 2.7 Spin-coated gecko setae array with PAA isolated layer on a silicon wafer 20

Figure 2.8 Fabricate (a) Computer-aided design (CAD) model for acrylic frame and (b) printed master mold with silicon wafer substrate in the acrylic frame 21

Figure 2.9 (a) Schematic of negative mold fabrication without surface treatment. (b) Negative PDMS mold with no treatment and trapped master mold (c) Master mold separated with tape and (d) Master mold separated with tweezer. (e) Negative PDMS mold damaged by tweezer. 22

Figure 2.10 (a) Negative PDMS mold with gold-sputtered and trapped master mold. (b) Master mold separated with tape and tweezer. 23

Figure 2.11 (a) Negative PDMS mold demolded from the master mold treated with PAA micropipette liquid deposition and (b) the separated master mold. 24

Figure 2.12 (a) Negative PDMS mold demolded from the master mold, treated with PEDOT: PSS micropipette liquid deposition, and (b) the separated master mold with the defect............. 24

Figure 2.13 (a) Cured negative PDMS mold before demolding and (b) separated master mold with defects. (c) Microstructured gaps in the negative PDMS mold and (d) the microstructures in the separated master mold.. 25

Figure 2.14 Schematic of the positive mold fabrication with defects.................................... 26

Figure 2.15 Replicated positive multi-design structure panel PDMS mold with no microstructures reserved. 27

Figure 2.16 (a) Angled view of replicated positive gecko setae array with defects and (b) angled view of the pilled off negative PDMS mold with trapped microstructures. 27

Figure 2.17 Modified tilted mushroom-shaped design (unit: μm)... 29

Figure 2.18 Schematic of the finalized negative and positive molds fabrication. 29

Figure 2.19 Negative mold of Modified tilted mushroom-shaped design. (a) Top view. (b) Cross-section view. 30

Figure 2.20 Positive mold of Modified tilted mushroom-shaped design. (a) Top view. (b) Cross-section view. 31

Figure 3.1 The isometric view of (a) SH (b) DH in CATIA.. 32

Figure 3.2 Isometric view of (a) MS (b) MD (c) WS, and (d) WD in CATIA....................... 33

Figure 3.3 Dimensions of the artificial seta in (a) MS and (b) WS (unit: μm). 34

Figure 3.4 Dimensions of the artificial seta in (a) MD and (b) WD (unit: μm)...................... 35

Figure 3.5 Surface of (a) aluminum plate and (b) silicon wafer scanned by a 3D profilometer. 36

Figure 3.6 Setup of the adhesion measurement 37

Figure 3.7 Linear regression of 50 g load cell calibration. 38

Figure 3.8 Schematic of the preload versus maximum adhesion test. 40

Figure 3.9 Schematic of the shear distance versus maximum adhesion test. 40

Figure 3.10 Adhesive performance of the uncleaned pure PDMS structure positive mold and the cleaned PDMS positive mold... 41

Figure 3.11 Adhesive performance of the cleaned pure PDMS positive mold on glass, aluminum plate and silicon wafer. 42

Figure 3.12 Adhesive performance of the SH and DH on glass, aluminum plate and silicon wafer. 43

Figure 3.13 Schematic of SH positive mold shear on glass. (a) Positive mold in contact with glass surface with zero preload. (b) 3.4 N preload was applied to the positive mold. (c) The positive mold moved toward right for 300 μm to shear the microstructures. 44

Figure 3.14 Adhesive performance of the SH and DH on glass, aluminum plate and silicon wafer with shear. 45

Figure 3.15 Adhesive performance of the MS, MD, WS and WD on glass 46

Figure 3.16 Adhesive performance of the MS, MD, WS and WD on the aluminum plate 47

Figure 3.17 Adhesive performance of the MS, MD, WS and WD on silicon wafer 47

Figure 3.18 Inclined front views of PDMS miniature microstructures. (a) MS design (b) MD design (c) WS design and (d) WD design. 49

Figure 3.19 Cross-section of PDMS miniature microstructures. (a) MS design (b) MD design (c) WS design and (d) WD design. 50

Figure 3.20 (a) Unrecoverable micro-pillars on the MS design when preload and shear were applied. (b) Propagated cracks on the WD design when preload and shear were applied. 51

Figure 3.21 COMSOL models of (a) MS and (b) MD in 3D. COMSOL models of (c) WS and (d) WD in 2D. 52

Figure 3.22 Geometry model of MS with mesh in COMSOL. 53

Figure 3.23 Contact pairs of MS in COMSOL. 54

Figure 3.24 (a) Fixed constraint on the lower block. (b) Symmetry on the geometry. 55

Figure 3.25 Von Mises stresses of compressed miniature microstructures in COMSOL. (a) MS design (b) MD design (c) WS design (d) WD design. 56

Figure 3.26 Ratio of effective contact area to total area during the compression. 57

LIST OF TABLES

Table 1.1 Designs of non-tilted artificial seta 6

Table 1.2 Designs of tilted cylinder-shaped and mushroom-shaped artificial seta 7

Table 1.3 Designs of wedge-shaped artificial seta.. 8

NOMENCLATURE

ADR	Active debris removal
RAB	Robotic-arm-based
SEM	Scanning electron microscope
H	Total height of the artificial seta
D	Diameter of the pillar
S	Center to center spacing
d	Diameter of the mushroom-shaped artificial seta
σ_a	Adhesion
UV	Ultraviolet
α	Fiber angle
β	Tip angle
θ_L	Large angle of wedge-shaped design
θ_S	Small angle of wedge-shaped design
PDMS	Polydimethylsiloxane
PUA	Polyurethane acrylate
2PP	Two-photon polymerization
PTFE	Polytetrafluoroethylene
PECVD	Plasma-enhanced chemical vapor deposition
C_4F_8	Octafluorocyclobutane
FDTS	1H,1H,2H,2H-perfluorodecyltrichlorosilane
FDM	Fused deposition modeling
MSLA	Mask stereolithography

PGMEA	Propylene glycol monomethyl ether acetate
PAA	Polyacrylic acid
PEDOT: PSS	Poly (3, 4-ethylenedioxythiophene) polystyrene sulfonate
RPM	Revolutions per minute
CAD	Computer-aided design
SH	Tilted mushroom-shaped design with same height
DH	Tilted mushroom-shaped design with different height
MS	Miniature tilted mushroom-shaped design with same height
MD	Miniature tilted mushroom-shaped design with different height
WS	Miniature wedge-shaped design with same height
WD	Miniature wedge-shaped design with different height
RMS	Root-mean-square

1 Introduction

From 1960 to 2010, the average number of objects sent to space was about one hundred per year [1]. With the development of aerospace engineering, the cost and process of sending satellites to space became cheaper and more accessible. The number of commercial objects in orbit significantly increased after 2010, and now, approximately 1750 objects are expected to be launched to space in one year. However, there are more than one million pieces of debris floating in space, and this number keeps increasing. Meanwhile, only about 30,900 debris objects are tracked [1]. Abundant space debris is roaming in the space environment, such as abandoned rocket stages, obsolete satellites, and particles from the collision of the objects in space. More than 15,000 satellites are planned to be launched, but space debris is a threat to all ~~the~~ operational satellites in the present and future [2]. Therefore, space debris has become an issue for future space tasks, and it is essential to actively reduce space debris to keep the space environment clean [1].

1.1 Gecko-inspired Dry Adhesion for Space Debris Removal

Several technologies for catching and removing space debris have been proposed and evaluated. Based on the feasibility analysis, four Active Debris Removal (ADR) methods are possible to be implemented to clean up the space environment in the future, which are laser-based, ion-beam shepherd-based, tether-based, and robotic-arm-based (RAB) [3]. Comparing the above four ADR methods, the RAB method is the most feasible technique. Regarding flexibility, the on-ground laser-based method has less range [3], but all the systems that rely on satellites actively approach space debris to remove them. In the aspect of cost, deploying the satellites that are integrated with a high-power pulsed laser generator [4], quasi-neutral plasma generator [5], or 5 to 10 km long tether [6] are more costly than the satellite with a robotic arm installed. Therefore, launching satellites with robotic arms that can attach to space debris and pushing them to deorbit will be the future of ADR missions.

Due to the challenge of the space environment, many traditional attachment methods for the robotic arm to grip objects are invalid. The shape and material of space debris are diverse, so the gripper based on friction, magnetic and/or electrostatic is unsuitable for ADR. Suction and Bernoulli grippers cannot be used in vacuum conditions. However, the dry adhesion gripper that utilizes van der Waals force, which is the intermolecular forces between particles, can adhere to nearly any close-contacted surface. The microstructures that are installed on the gripper can produce dry adhesion to attach space debris firmly [7].

In nature, the gecko is the animal that relies on van der Waals forces to climb. Multiple length scales of elements are spanned in the gecko’s adhesive system. Geckos have four legs, and each leg has five toes as Figure 1.1(a) shown. The toes have rows of flaps called lamellae, which are visible to the naked eye, are showing in Figure 1.1(b). Each lamellae is covered with arrays of microscale hair-like seta [8]. The terminal of a single seta is divided into hundreds of nano-scale spatula-shaped nanostructures [9]. The hierarchical multiscale with nanostructured terminals on gecko feet can conform to the contact surface to induce van der Waals forces [10]. By imitating the complex structure of gecko’s feet and installing the reproduced structures on the robotic arms of the satellites, the capability of robotic-arm-based satellites to remove space debris can be proven in the future.

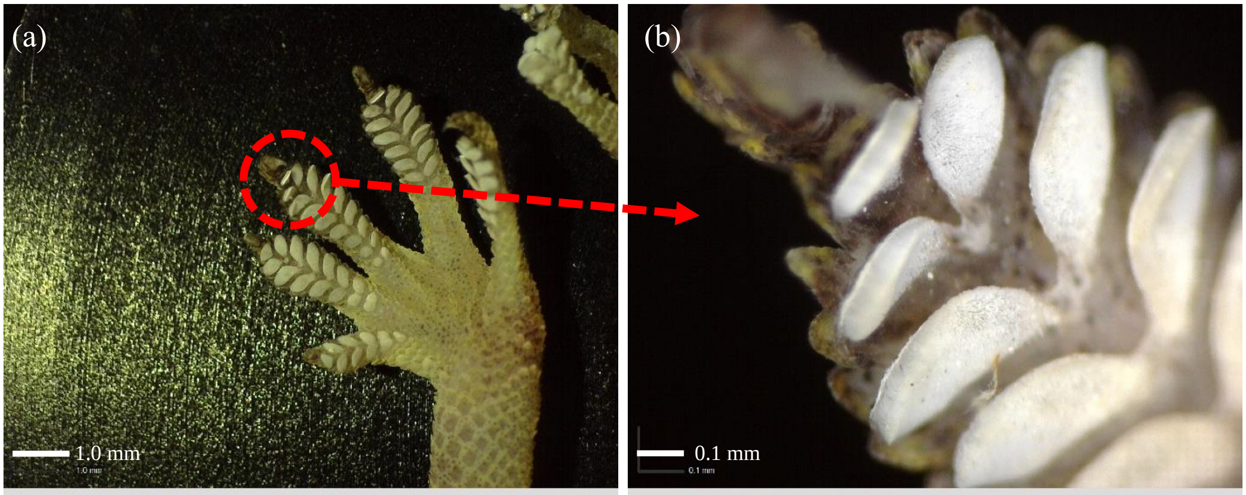

Figure 1.1 (a) Gecko’s foot and (b) detail view of its toe.

1.2 Gecko-inspired Dry Adhesion Microstructure

Reproducing a copy of gecko feet is challenging due to the difficulty of nanoscale fabrication and complicated hierarchical structure. The surface roughness of common material surfaces can act on both macroscale and microscale [11]. The designs of gecko-inspired dry adhesion systems can imitate the setae arrays of gecko toes to induce van der Waals force when it closely contacts a surface. The magnitude of van der Waals force is sensitive to the distance between two particles [12], and the adhesive force of gecko-inspired dry adhesion microstructures is given by the van der Waals force produced by the artificial setae. The key to achieving a microstructure with high adhesion is to increase the effective area of the artificial setae arrays in contact with surfaces.

The shape design of a single artificial seta mainly is cylinder-shaped [13, 14], mushroom-shaped [15, 16] or wedge-shaped [17, 18]. A cylinder-shaped artificial seta is the most straightforward design for imitating the gecko seta. According to Ref [13], the cylinder-shaped seta was fabricated by covering a mask aligner on a thin layer of photosensitive resin. The mask aligner had a circular holes pattern, and the photosensitive resin is solidified to become cylinder-shaped by irradiation. On the other hand, mushroom-shaped artificial seta has higher adhesion strength, because the geometry of the tip avoids stress concentration at the contact boundary [13]. To have the controllability of switching between attachment and detachment, the design of artificial seta needs to be tilted. The tilted artificial seta provides strong adhesion when it shears along the tilted direction while contacting the surface, and easily detach via reversing the shear direction [19, 20]. Besides the tilted cylinder-shaped and the tilted mushroom-shaped artificial seta designs, wedge-shaped artificial seta designs also have the ability to provide controllable adhesion through shear motion [21]. For example, in Figure 1.2, the tilted designs show shown strong adhesion is active while the tilted microstructure is in contact with a surface and shift toward the left. The adhesion can be reduced by shifting the microstructure back to neutral position or shifting to release mode.

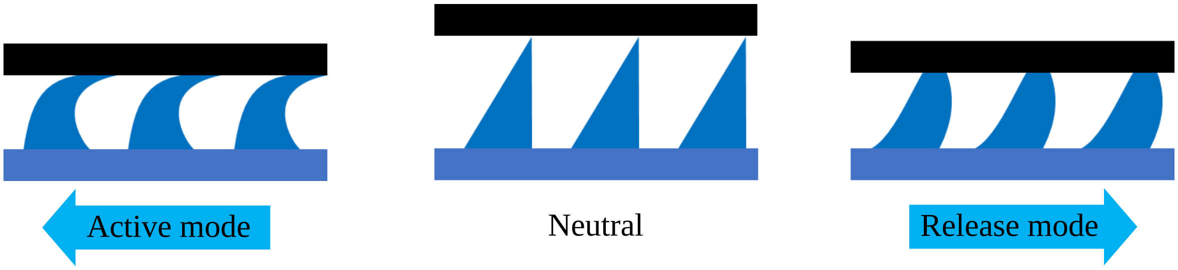

Figure 1.2 Example of active mode and release mode of the wedge-shaped artificial seta designs.

1.2.1 Non-tilted artificial seta

There are two major kinds of non-tilted artificial seta: cylinder-shaped and mushroom-shaped. The advantages of the non-tilted cylinder-shaped design are low fabrication difficulty and less structural design parameters [14, 22]. However, many studies showed that non-tilted cylinder-shaped designs had lower adhesion than non-tilted mushroom-shaped designs, due to the high stress concentration on the edge of the contact area during detachment [23]. By modifying the shape of the tip of the cylinder-shaped artificial seta, mushroom-shaped artificial seta is designed to lower the high stress concentration on the edge of the contact area, so that the adhesion performance of the microstructure can be enhanced. The example of the non-tilted cylinder-shaped and mushroom-shaped artificial seta designs are shown in Figure 1.3.

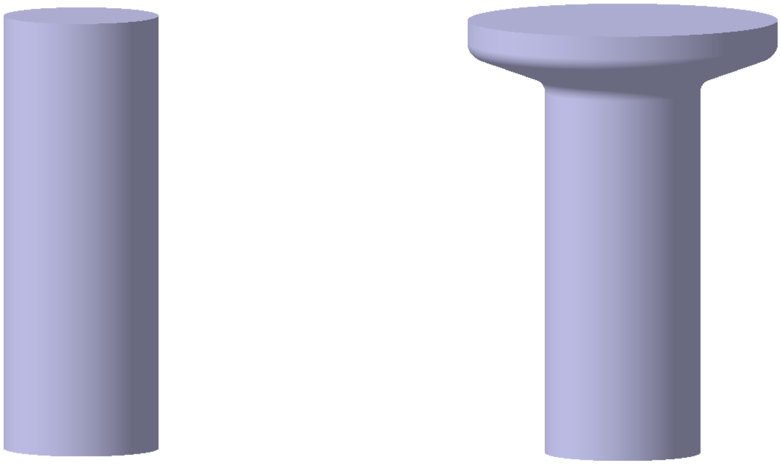

Figure 1.3 Example of the non-tilted cylinder-shaped and mushroom-shaped artificial seta designs.

The shape, material, dimensions, and adhesion of the non-tiled artificial seta array are shown in Table 1.1. The total height of the artificial seta, *H*, ranges from 9.4 to 100 μm, and the average height is about 30 μm. The diameter of the pillars, *D*, varies between 2.5 to 19.5 μm. The center to center spacing of the artificial seta, *S*, is typically 2 to 3 times the diameter of the pillars. The tip diameter of the mushroom-shaped artificial seta, *d*, is slightly wider than the diameter of the micropillars. The adhesions of different designs, σ_a, are also listed in Table 1.1 below.

Table 1.1 Designs of non-tilted artificial seta

Shape	Material	Height (*H*) [μm]	Diameter (*D*) [μm]	Spacing (*S*) [μm]	Tip Diameter (*d*) [μm]	Adhesion (σ_a) [N/cm^2]	Reference
Cylinder	Sylgard 184	30	10	-	-	2.3	[15]
	PUA/Fe3O4	20	2.5	6	-	9	[13]
	Epoxy polymer	20	9	11	-	1	[14]
	CaCO$_3$ NPs PDMS	35	40	80	-	4.4	[16]
	SU-8	48	25	40	-	~3	[22]
	SU-8	100	25	40	-	~3.8	
Mushroom	Sylgard 184	20	7	-	10	21.9	[15]
	PMMA	47.8	13.4	~20	14.4	0.175	[24]
	Sylgard 184	9.4	19.5	40	33.6	27	[25]
	PDMS	18	10	32	~13	6.8	[23]
	Sylgard 184	10	11.1	-	17.1	20	[26]
	Sylgard 184	19	-	-	10	10	[27]
Notes: Estimated values are indicated by tildes, ~. Non-reported values are indicated by dash, -							

Among cylinder-shaped seta materials, the mixture of ultraviolet (UV) curable polyurethane acrylate (PUA) and Fe_3O_4 nanoparticles has the highest adhesion with 9 N/cm^2. The non-uniform distributed nanoparticles make the root of the artificial seta stiffer [13]. The cylinder-shaped artificial seta that is made of epoxy polymer has the lowest adhesion with 1.0 N/cm^2 [14]. The adhesive performance of cylinder-shaped artificial seta ranges from 1 to 9 N/cm^2, and the average adhesion is 6.5 N/cm^2.

The mushroom-shaped artificial seta has two notable characteristics. The material used is mainly PDMS, and the adhesion performance is better than the cylinder-shaped artificial seta. The adhesive performance of mushroom-shaped artificial seta ranges from 0.175 to 21.9 N/cm^2.

1.2.2 Tilted artificial seta

The tilted artificial seta, also known as anisotropic structures, have the advantage of actively switching between attachment mode and detachment mode by shearing the tilted artificial seta along or against the tilted direction [28]. The adhesive performance drastically decreases when the tilted artificial seta is against the tilted direction [2]. As the tilted cylinder-shaped artificial seta adheres to the surface with its flat terminal, the mushroom-shaped artificial seta attaches to the surface with its tilted panel. Unlike the pillar-like structures that attach to the surface with their terminal panel, the wedge-shaped artificial seta attaches to the surface with its side surface.

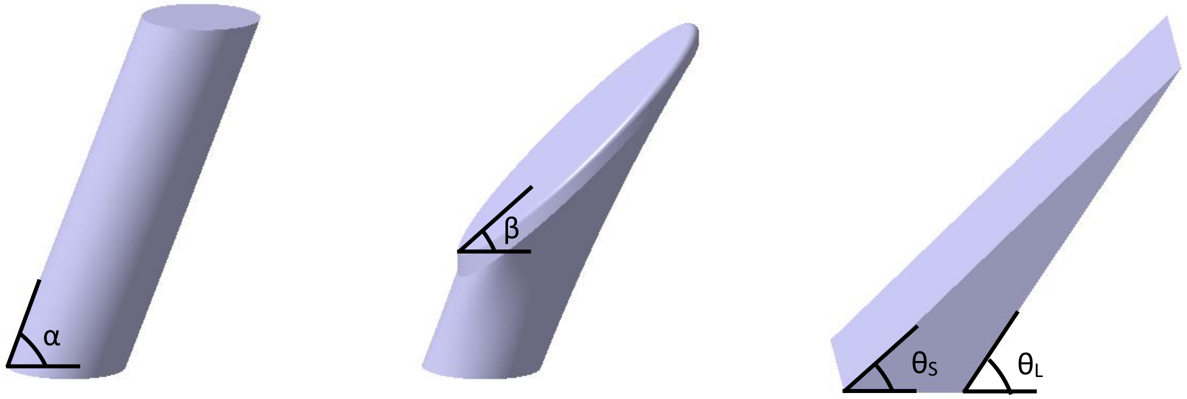

Figure 1.4 Example of tilted microstructure designs. (a) Tilted cylinder-shape design. (b) Tilted mushroom-shape design. (c) Wedge-shaped design.

In Table 1.2, the shape, material, dimensions, and adhesion of the tilted cylinder-shaped and mushroom-shaped artificial seta array are listed. As Figure 1.2 shown, the fiber angle, α, is the angle between the pillar and substrate, and the tip angle, β, represents the angle between the tilted panel and substrate.

Table 1.2 Designs of tilted cylinder-shaped and mushroom-shaped artificial seta

Shape	Material	Height (*H*) [μm]	Diameter (*D*) [μm]	Spacing (*S*) [μm]	Tip Diameter (*d*) [μm]	Fiber Angle (*α*) / Tip Angle (*β*) [deg]	Adhesion (σ_a) [N/cm^2]	Reference
Cylinder	SU-8	100	25	40	-	72 / 0	2.5	[22]
Mushroom	PUR	100	35	120	-	34 / 14	10	[19]
	PUR	92	19	40	-	70 / 0	0.6	[29]
	Sylgard 184	270	100	130	280	70 / 45	~1	[30]
	silicone rubber	1000	300	1000	380	70 / 45	~0.25	[31]
Notes: Estimated values are indicated by tildes, ~. Non-reported values are indicated by dash, -								

Table 1.3 Designs of wedge-shaped artificial seta

Material	Height (H) [μm]	Width (W) [μm]	Length (L) [μm]	Large Angle (ϑ_L) [deg]	Small Angle (ϑ_S) [deg]	Spacing (S) [μm]	Adhesion (σ_a) [N/cm^2]	Reference
PDMS	200	50	50	90	76	-	0.5	[21]
PDMS	80	20	200	90	76	40	1.8	[32]
Sylgard 184	13	8.5	-	75	62	-	0.94	[33]
Sylgard 184	~29	50	-	90	30	50	~0.8	[34]
Sylgard 184	~58	100	-	90	30	100	~0.45	
Sylgard 184	~87	150	-	90	30	150	~0.35	
Sylgard 184	~138	100	-	90	54	100	~0.45	
Sylgard 184	~97	100	-	90	44	100	~0.3	
Notes: Estimated values are indicated by tildes, ~. Non-reported values are indicated by dash, -.								

In Table 1.2 and Table 1.3, most of the adhesions of tilted design are significantly lower than the non-tilted artificial seta in Table 1.1. The tilted microstructure design sacrifices the maximum adhesion to obtain controllability on adhesion through shear motion. In addition, by comparing the adhesive performance within the tilted structure, mushroom-shaped artificial seta is generally better than cylinder-shaped and wedge-shaped.

1.3 Design Parameters

The spectrum of the design of artificial seta is broad due to the numerous combinations of materials, sizes, tilted angles, aspect ratio, and spacing distances. As far as the author's knowledge, no optimized design or general equation of approximation for estimating the resultant adhesive force exists. In this work, the effects of different design parameters are discovered with experimental results to properly design the artificial seta.

1.3.1 Material

The nanoarray of hundreds of spatulae is made from β-keratin, which has approximately 2 GPa modulus of elasticity [35]. The commonly used material in gecko-inspired microstructure with a similar modulus of elasticity is epoxy. Due to the poor flexibility, the epoxy polymer is unsuitable for complex designs. As Table 1.1 shown, epoxy was generally used to fabricate cylinder-shaped artificial seta, and the performance in adhesion is commonly poorer than the design manufactured with other materials. Using the material with the highest viscoelastic behavior is suggested to improve the adhesion performance of gecko-inspired microstructure [14].

Another study shows that the adhesion of gecko-inspired microstructure can be increased by reducing Young's modulus of the material [34]. One of the commonly used materials that have lower Young's modulus for gecko-inspired dry adhesive surfaces fabrication is polydimethylsiloxane (PDMS). Sylgard 184 is one PDMS with Young's modulus of 1.8 MPa [27, 32, 33]. It is an ideal material for gecko-inspired dry adhesive surfaces due to its low surface energy and environmental sensitivity [28, 36].

1.3.2 Tilted angle

The angle between the tilted setae and the lamella on the gecko toe was about 45° [37]. Some designs imitated the tilted tip of real gecko setae, and the resulting adhesion was between 0.25 to 1 N/cm^2 [30, 31]. Another study found that the wedge-shaped artificial seta with a 30° incline angle has greater adhesion than 44° and 54°. The effects of tilted angles of the pillar and panel are not reported yet due to the tiled angle, size, and dimension coupling. When the tilted angle is changed, the height and the aspect ratio of the right angle wedge-shaped are changed accordingly [34].

1.3.3 Sizes, Aspect Ratio, and Spacing

Due to the intimate contact between its nanoscale spatulae and the rough surfaces, a gecko can make hold of its body mass on the ceiling walls [38]. However, for the artificial gecko-inspired microstructure, the microscale fibrillar structure cannot closely contact the rough surface without a void, which introduced an initial crack in the adhesive system. As the size of the artificial seta decreases, the adhesion of the gecko-inspired microstructure was enhanced due to the lesser initial crack [39, 40]. To ensure that all the artificial setae can contact the rough surface, the height of the artificial seta should be much greater than the roughness of the surface. From Table 1.1 to Table 1.3, all the heights of artificial seta are greater than 10 μm, and the average height is about 70 μm (excluding the design with 1000 μm height).

Generally, the artificial seta with a higher aspect ratio performs better in adhesion [14, 15]. However, the artificial seta was adhered to the neighbor seta when the aspect ratio ~~is~~ was too high, and the adhesive performance ~~is~~ was reduced as the artificial setae started clustering [48]. The recommended aspect ratio between height and diameter of the artificial seta ranges from 2 to 3, which has better adhesive performance than a low aspect ratio design and avoids clustering [14, 15, 40].

1.4 Fabrication Process

In general, the artificial seta microstructures are mainly fabricated from mold casting. There are mainly two ways to produce the mold: micromachine and lithography [28]. Micromachine is used to manufacture the wedge-shaped artificial setae surface. A microtome blade was used to cut the wax mold [32, 41]. For a conventional UV lithography process, firstly, the curable resin was spin-coated on a substrate with desired thickness and covered with a mask that had a micropattern. The uncovered curable resin was solidified under UV light, and the residual uncured resin was rinsed. However, this conventional UV lithography process has limitations in designing complex microstructures and is used to fabricate cylinder-shaped artificial setae [22, 42]. To produce the artificial seta with a more complicated design, Two-Photon Polymerization (2PP) 3D printing was used to fabricate the microstructure mold. The photosensitive resin was subjected to two near-infrared photons and polymerized [43]. With the advantages of high resolution and accuracy, microstructures with complicated overhanging designs can be produced [30, 44]. Once the molds are fabricated, PDMS or epoxy was poured onto the mold and cured. The desired microstructure was obtained when demolded.

For microstructures that have overhanging features or high aspect ratios, direct demolding may damage the microstructures. A separation layer is needed to isolate the cured PDMS or epoxy and the molds. For example, a plasma etcher is used to deposit a layer of polytetrafluoroethylene (PTFE) on the mold by plasma-enhanced chemical vapor deposition (PECVD) with octafluorocyclobutane (C_4F_8) [30]. In addition, a layer of 1H,1H,2H,2H-perfluorodecyltrichlorosilane (FDTS) can also be deposited on the mold as a separation layer with oxygen plasma [33].

1.5 Motivations

Space debris has been a growing concern in the space exploration sector. To combat this issue, biomimicry can create a gecko’s feet microstructure that will be attached to a gripper or robotic arm. This will enable the capture of debris through dry adhesive microstructure. However, producing such microstructures is expensive and complex, hindering their implementation. Moreover, the gecko-inspired dry adhesive microstructure design is not fully optimized. In terms of adhesive performance, no study has compared and concluded the best shape design for tilted microstructures, such as wedge-shape or tilted mushroom-shape. In addition, the produced artificial setae microstructures have uniform heights [22, 30], and the effect of alternating height artificial setae microstructures has not been accessed yet.

1.6 Objectives

The objective of the demonstrated thesis is to develop an advanced and cost-effective fabrication process to produce a simplified gecko-inspired microstructure with 2PP and polymer molding, aiming to improve the adhesive properties of the microstructures. In addition, the adhesive performance of wedge-shaped and mushroom-shaped microstructures will be compared. Meanwhile, the effect of alternating heights on the gecko-inspired microstructure will be explored.

2 Microstructures Fabrication Process

This section describes the process of designing, printing, coating, and fabricating the molds. The master molds, which consisted of multiple microstructures, were designed in CATIA V5 and printed with a negative photoresist (IP-Q, Nanoscribe, Germany) using a 2PP printing technique with Photonic Professional GT2 (Nanoscribe, Germany). Different coating materials and techniques were applied to the printed master molds to seek a cost-effective process for fabricating negative molds and positive molds.

2.1 Microstructure Design

A few design factors were considered for fabricating artificial gecko setae, such as the resolution of the different heights, printability of thin and tall structures, and overhanging. As shown in Figure 2.1, four different structures were designed to examine the above; (a) step-structure design with $250 \times 200 \times 250$ μm^3 in XYZ direction to study the effects of different shapes and depth on adhesion, (b) two-wall design with $20 \times 200 \times 250$ μm^3 in XYZ direction and 20 μm gap to investigate the effects of distance between structures, (c) 50 μm thick plane rectangular standard shape for comparison, and (d) an artificial gecko seta design with a height of 250 μm, consisting a disk with a diameter of 220 μm and thickness of 20 μm and a cylinder with a diameter of 100 μm. The substrate of the multi-design structure panel is $650 \times 650 \times 20$ μm^3 in the XYZ direction. The drawing of individual structures with dimensions is shown in Figure 2.2.

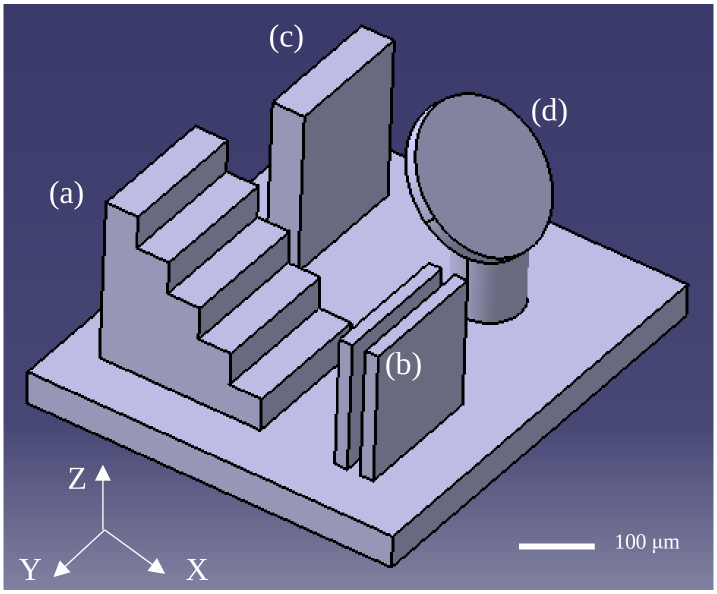

Figure 2.1 CATIA model of multi-design structure panel. (a) Step-structure design. (b) two-wall design. (c) Thick plane rectangular standard shape. (d) Sample of artificial gecko seta design.

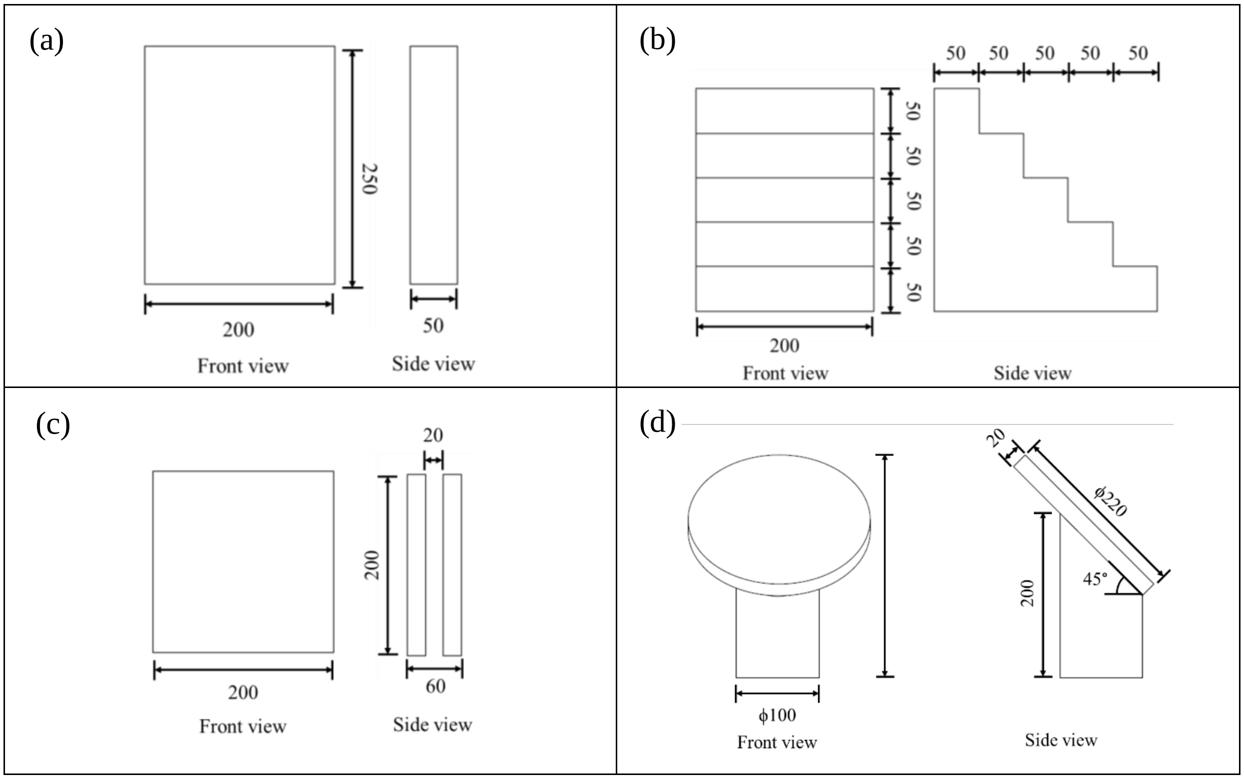

Figure 2.2 The drawing of individual structures in multi-design structure panel with dimensions. (a) Thick plane rectangular standard shape. (b) Step-structure design. (c) Two-wall design. (d) Sample of artificial gecko seta design.

In addition, four tilted mushroom-shaped artificial setae structures were reproduced to study the adhesion performance. The dimensions of the mushroom-shaped artificial setae are referenced from the study of Busche *et al.* [30], which is the first paper on using the 2PP technique to fabricate artificial gecko setae.

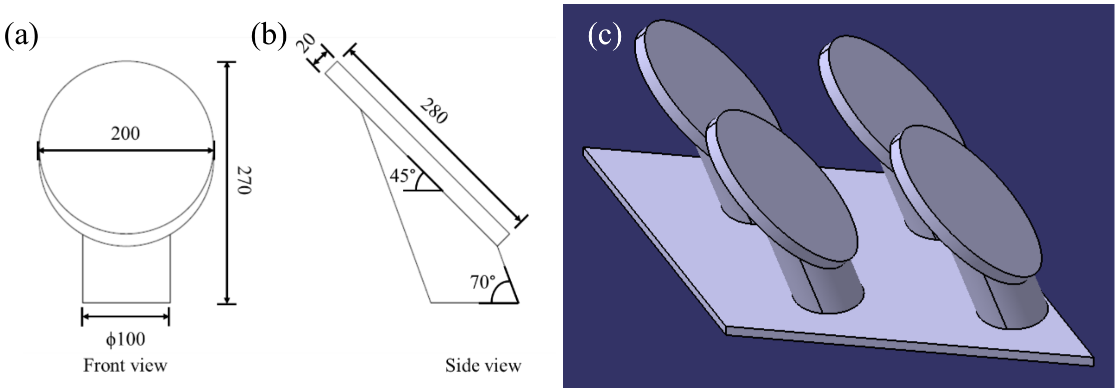

Figure 2.3 Tilted mushroom-shaped design from Busche *et al.* [30]. (a) Front view. (b) Side view (unit: μm). (c) Isometric view in CATIA.

2.2 Printing Microstructure Master Mold

As per the design requirement, the microstructure must be flexible, and the thinnest feature was 20 μm. Traditional fused deposition modeling (FDM) printing machine, which was able to print flexible filaments, cannot print microstructures due to the limits of filament, step motors, and nozzle diameter. Even though the mask stereolithography (MSLA) printing machine could print flexible material by curing resin with UV light, the resolution was not capable of printing the desired structure. To acquire a flexible microstructure, the rigid master mold printed using 2PP was cast with PDMS to create the negative mold, and the negative mold was then used to fabricate the positive mold out of PDMS. In terms of the cost and efficiency, the printing process was time-consuming and expensive by comparing with casting molds. A 1 cm by 1 cm area of the desired microstructure took about 8 hours to print, and the cost of the photoresist was relevantly higher than PDMS in unit volume. The material and the operation fee of the 2PP machine were expensive. Therefore, fabricating the molds from the printed structure was essential to ensure that the desired microstructure could be mass-produced. In addition, a mold with larger areas could be obtained by casting PDMS on the array consisting of multiple smaller PDMS negative molds.

The microstructure master mold was printed with a negative photoresist in a 2PP machine. A clean silicon wafer with a drop of photoresist in the center was placed inside the printer. Using the 2PP process, the designed microstructures were printed with 100 mm/s scan speed and 100% laser power. The printed microstructure was developed in 1-methoxy-2-propanol acetate (PGMEA) (Merck, Germany), rinsed with isopropanol, and dried with an air blower ball. The printed microstructure was exposed to 405 nm UV light for 30 minutes to cure the photoresist fully. As shown in Figure 2.3, the quality of printed molds was determined with a digital microscope (Dino-Lite Edge, AnMo Electronics Corporation, Taiwan). An 8 by 8 array of multi-design structure panels was printed on a silicon wafer with 1000 micrometer in X and Y direction spacing, as seen in Figure 2.3 (a). The printing quality of four shapes array was acceptable. The step-structure had a clear transition in alternating heights, and the thick plane rectangular standard shape stood straight. The overhanging feature on the sample of artificial gecko seta can be printed with 2PP. However, when printed, the two-walled structure did not maintain a constant separation distance. Figure 2.3 (b) showed the gecko setae unit panel with an array of 19 × 25 (in XY direction) to fit the 1 centimeter by 1 centimeter area of the center of the silicon wafer.

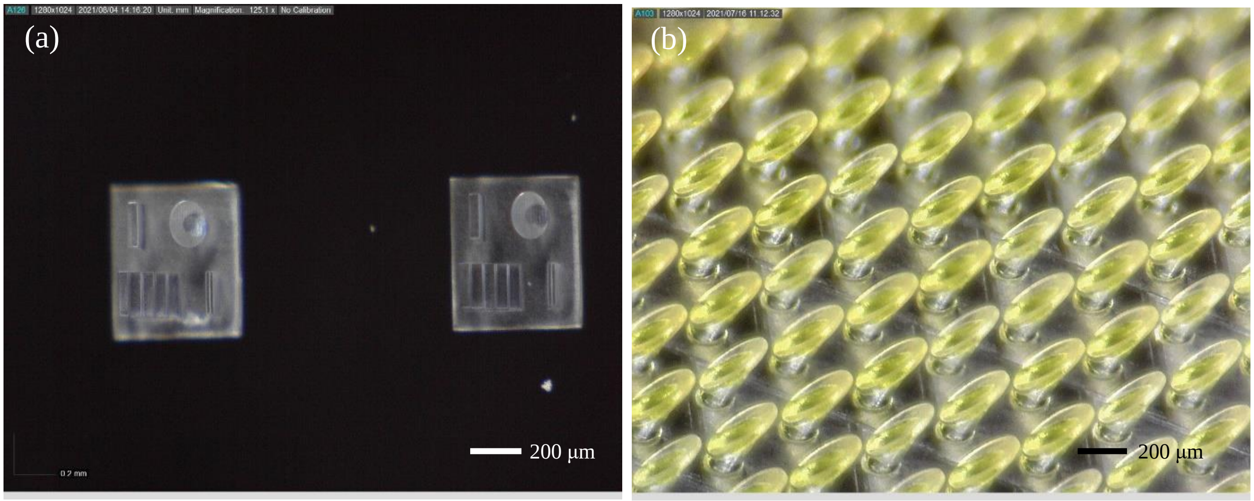

Figure 2.4 Printed master molds on silicon wafer. (a) Top view of multi-design structure panel array. (b) Angled view of artificial gecko setae array.

2.3 Surface Treatment

The steps below describe different master mold surface treatment processes. The following surface treatments had the potential to keep the printed master mold from sticking to the negative mold during the detaching process. Three deposition techniques are purposed to form a separation layer onto the printed master molds: gold sputtering, micropipette liquid deposition, and spin coating. Due to the excellent malleability of gold sputtering, a thin layer of gold on the printed master mold might help detach the negative mold without destroying the printed master mold. Otherwise, both polyacrylic acid (PAA) and poly (3, 4-ethylenedioxythiophene) polystyrene sulfonate (PEDOT: PSS) formed an isolated layer when dried, and they were soluble in water. Applying PAA or PEDOT: PSS on the printed master with micropipette liquid deposition or spin coating might ensure that only the PDMS mold would be detached, but the layers could be washed out with water. However, PAA was much thicker than PEDOT: PSS, so 5% PAA was prepared by diluting 1 gram of PAA with 6 grams of isopropanol to decrease the viscosity of PAA.

2.3.1 Gold Sputtering

The microstructure was placed in a sputter coater (108 Manual, Ted Pella, USA) to coat with gold for 30 seconds with 30 milliamps (mA) current and 0.08 millibars Argon gas pressure. The gold layer fully covered the exposed microstructure surface, as seen in Figure 2.4. However, the surfaces within the two-wall design could not be inspected.

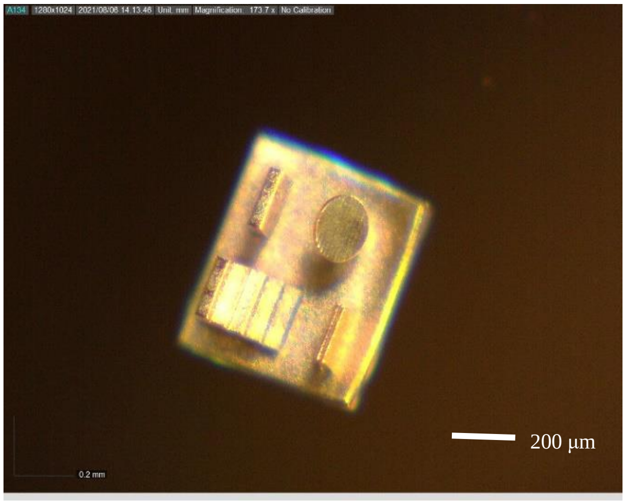

Figure 2.5 Multi-design structure panel treated with gold sputtering

2.3.2 Micropipette Liquid Deposition

5 microliters (µL) of 5% PAA were dropped on two multi-design structure panels with PEDOT: PSS dropped on the other two multi-design structure panels. The microstructure was dried at room temperature for 1 hour. The PAA layer fully covered the multi-design structure panel when the 5 µL of 5% PAA was dried, as shown in Figure 2.5 (a). A Curved PAA layer was formed at the sharp edges of the microstructure. Dried PEDOT: PSS layer in Figure 2.5 (b) also had the same issue, but the edge of the microstructure was more distinct.

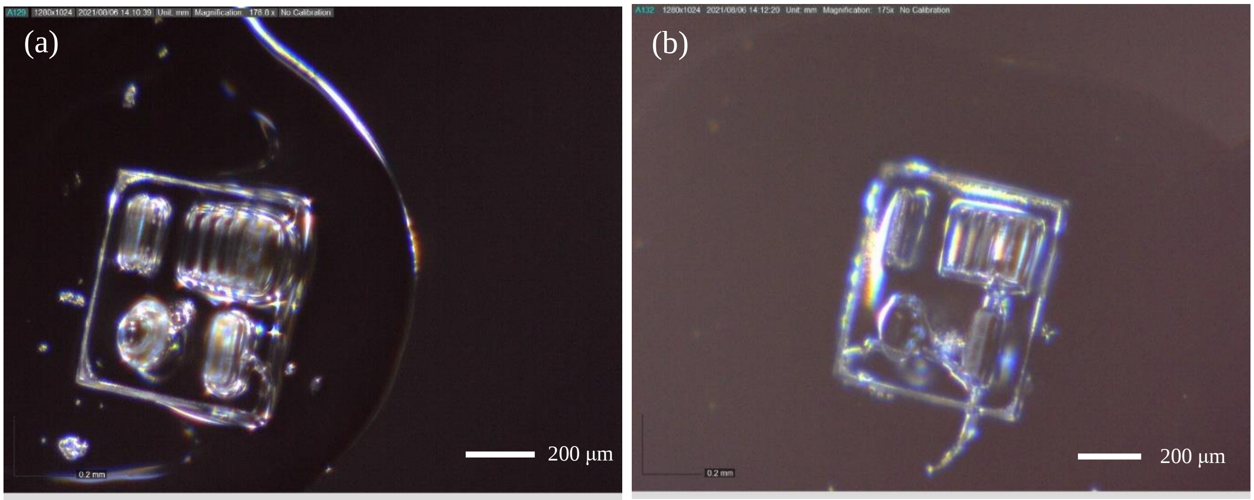

Figure 2.6 Multi-design structure panel treated with 5 microliters of (a) 5% Polyacrylic acid and (b) PEDOT: PSS

To obtain a better quality of the PAA layer and PEDOT: PSS layer, the excess liquid, which gathered at the sharp edge of the microstructures, needed to be removed. Therefore, the spin coating was introduced to form a uniform layer of PAA and PEDOT: PSS.

2.3.3 Spin Coating

The procedure consisted of covering the master mold with 5% PAA and spin-coating the same for 60 seconds at 2000 RPM. PEDOT: PSS was not spin-coated due to the poor quality of the detached molds from the micropipette liquid deposition process. Additional reasons for not spin-coating PEDOT: PSS will be discussed in section 2.4.3.

When the layer of 5% PAA was dried out, the surface of the gecko setae array was determined to be fully covered by PAA as Figure 2.6 shows. Spin-coating did not affect or damage the microstructures at 2000 revolutions per minute (RPM), while the extra 5% PAA was removed.

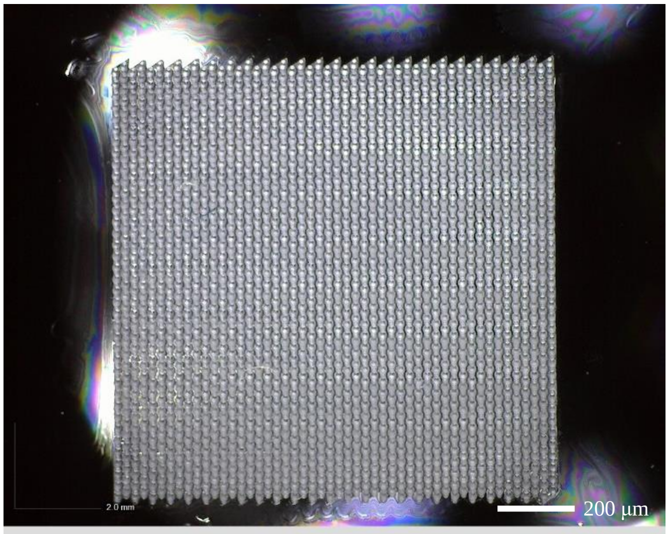

Figure 2.7 Spin-coated gecko setae array with PAA isolated layer on a silicon wafer

2.4 Fabrication of Negative Molds and Positive Molds

Negative PDMS molds were fabricated by pouring PDMS onto an acrylic frame, which had the printed master molds installed, and detaching after PDMS was cured. A PDMS mold for the uncoated master mold was fabricated as a control group. The defects of the negative PDMS molds and printed master molds were inspected with a digital microscope.

The 2 inches diameter silicon wafer, which carried the printed master mold was placed and locked in an acrylic frame, as shown in Figure 2.7. A cubic hole was surrounded by four pieces of acrylic blocks, as shown in Figure 2.7 (a). The PDMS used in this experiment was Sylgard® 184 and was mixed in a 10:1 ratio of base to curing agent. The printed master molds were placed in the center of the cubic hole, and the hole was filled with PDMS. The negative mold was acquired by curing PDMS at 90 °C for 12 hours in a vacuum chamber at 700 mmHg. The replicated positive mold was fabricated from the negative mold with the same procedure for pouring and curing the negative mold.

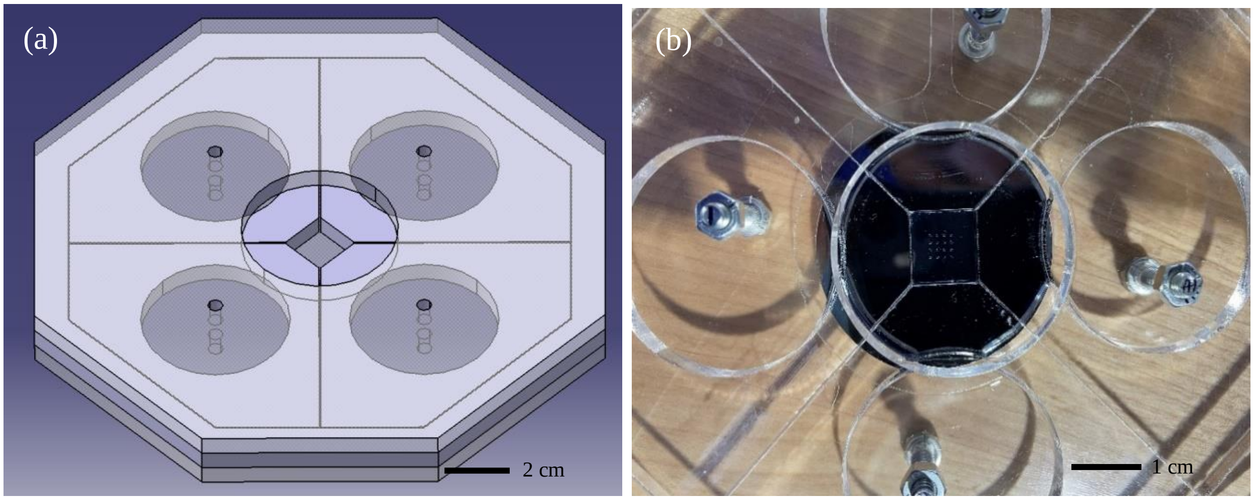

Figure 2.8 Fabricate (a) Computer-aided design (CAD) model for acrylic frame and (b) printed master mold with silicon wafer substrate in the acrylic frame

2.4.1 No Surface Treatment

Without surface treatment on the master mold, the printed structure was stuck in the PDMS negative mold during the demolding process. Only one of the structures in the multi-design structure panel array was separated from the PDMS negative mold with tape, but the demolded structure was not completed. The rest of the structures without surface treatment were pulled off with tweezers. However, none of the master molds could be separated without damaging the structure. The negative PDMS mold sustained damage when tweezers were utilized. Therefore, the master mold must be treated to achieve demolding without damaging the negative mold and master mold.

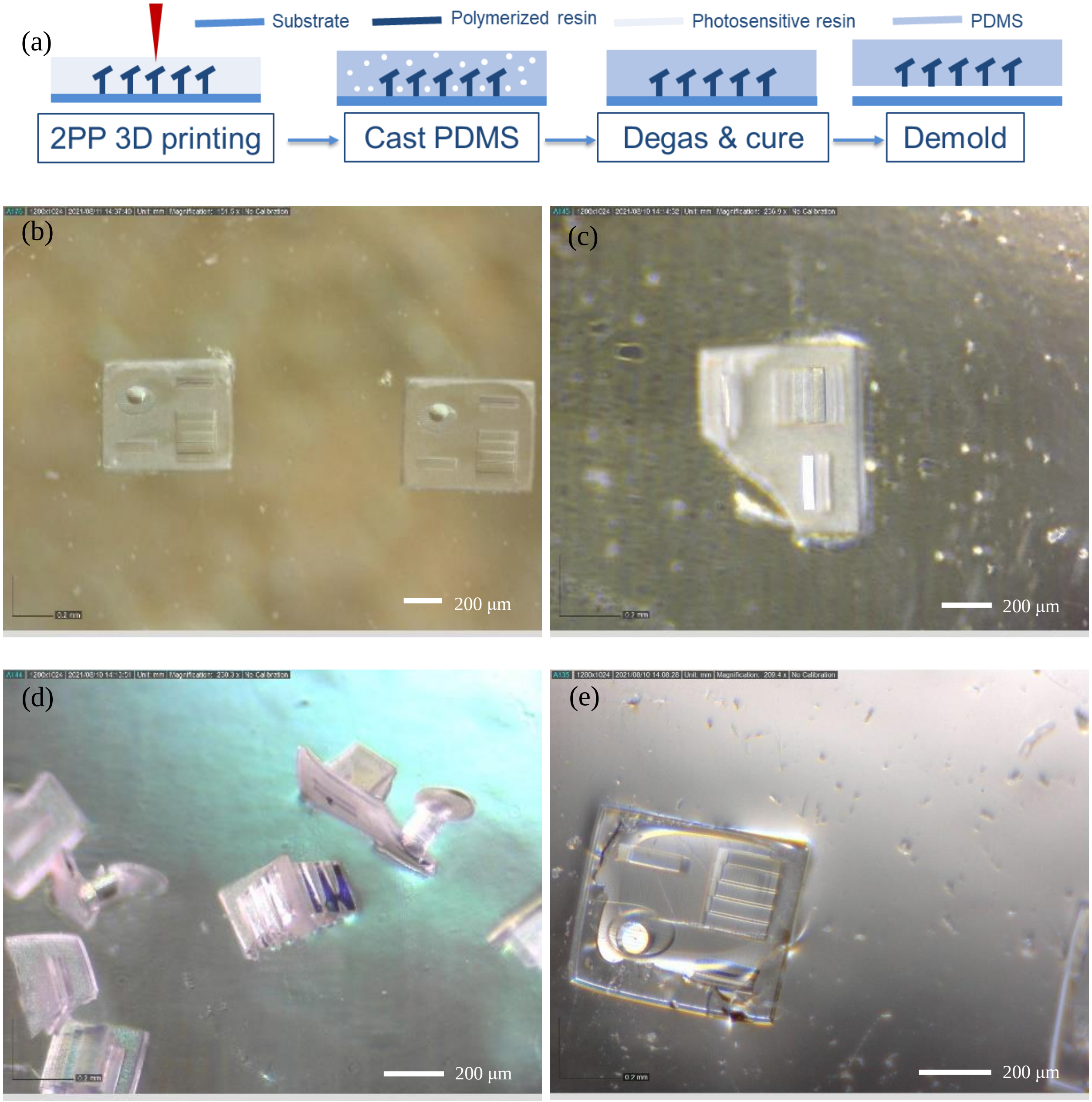

Figure 2.9 (a) Schematic of negative mold fabrication without surface treatment. (b) Negative PDMS mold with no treatment and trapped master mold (c) Master mold separated with tape and (d) Master mold separated with tweezer. (e) Negative PDMS mold damaged by tweezer.

2.4.2 Gold Sputtering

The master mold structures covered by gold adhered to the PDMS negative mold during the demolding process. The master mold could not be demolded with tape, and the tape could only peel off most of the gold from the PDMS negative mold surface. Additionally, by using tweezers, it was impossible to demold the entire master mold structures from the PDMS negative mold.

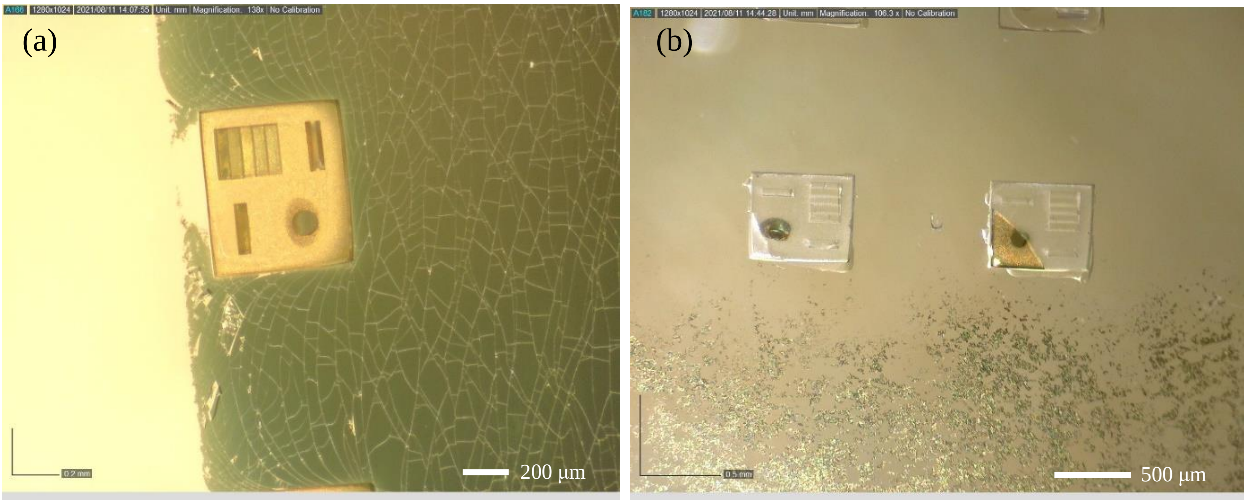

Figure 2.10 (a) Negative PDMS mold with gold-sputtered and trapped master mold. (b) Master mold separated with tape and tweezer.

2.4.3 Micropipette Liquid Deposition

The master mold structure treated with 5 microliters of 5% PAA was successfully demolded from the PDMS negative mold. The master mold structure was demolded in one piece without damage, and the PDMS negative mold quality was acceptable. As Figure 2.11 shown, due to the PAA isolate layer, a uniform layer was not formed as the PDSM negative mold had wrinkles surrounding the microstructure.

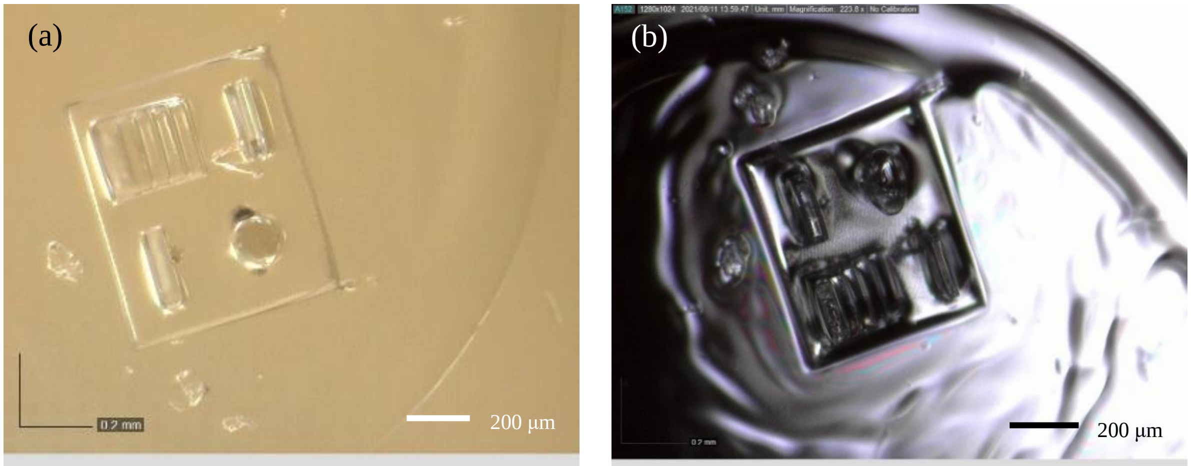

Figure 2.11 (a) Negative PDMS mold demolded from the master mold treated with PAA micropipette liquid deposition and (b) the separated master mold.

The master mold structure treated with 5 microliters of PEDOT: PSS was successfully demolded from the PDMS negative mold. The circular panel of the multi-design panel in the master mold structure was damaged during the demolding process as Figure 2.11 shown, but the broken pieces did not remain in the negative PDMS mold. The surface of the PDMS negative mold that surrounded the microstructure was even when comparing the surface, as shown in Figure 2.10 (a) and Figure 2.11 (a).

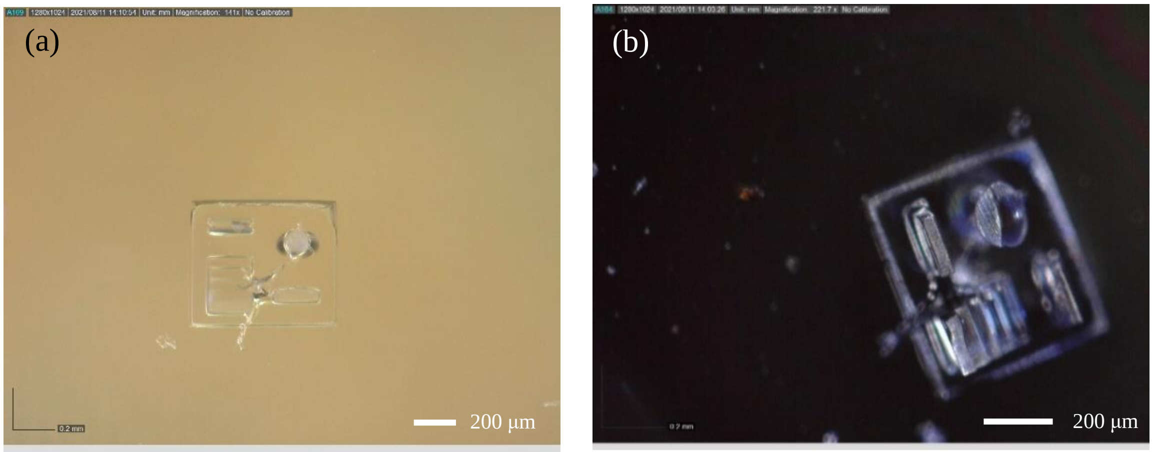

Figure 2.12 (a) Negative PDMS mold demolded from the master mold, treated with PEDOT: PSS micropipette liquid deposition, and (b) the separated master mold with the defect.

2.4.4 Spin Coating

About 5% of the gecko setae array structure was missing during the demolding process, as shown in Figure 2.13 (b) and (d), but most of the printed design remained on the silicon wafer. Unevenly applied force to separate the negative mold might be why most of the missing structures occur at the border of the master mold. The negative PDMS mold had even surfaces when the master mold was spin-coated with 5% PAA as Figure 2.13 (c) shows. There were minor defects due to the dust in the printed microstructure before casting PDMS. The negative PDMS mold demolded from the microstructure favorably when the master mold was spin-coated with 5% PAA.

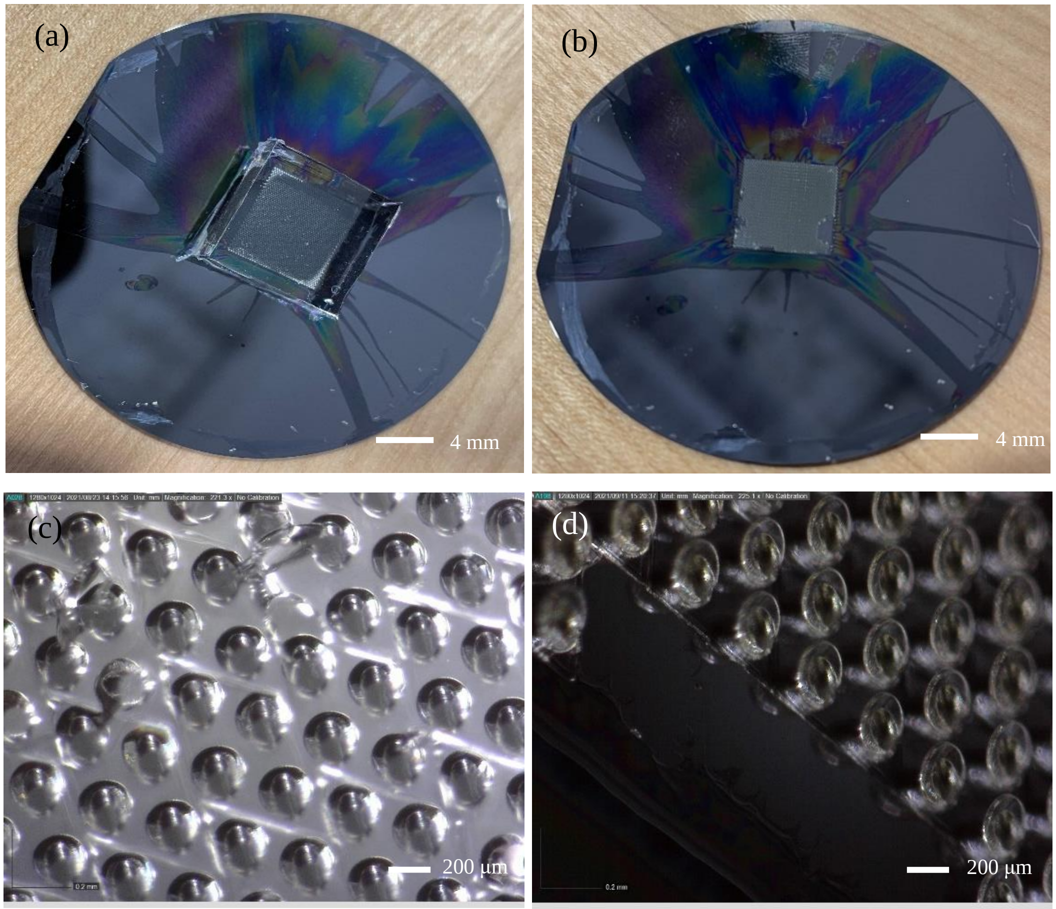

Figure 2.13 (a) Cured negative PDMS mold before demolding and (b) separated master mold with defects. (c) Microstructured gaps in the negative PDMS mold and (d) the microstructures in the separated master mold.

2.4.5 Replicated Positive Mold

The positive mold of the multi-design structure and gecko setae array was fabricated by pouring PDMS onto an acrylic frame with a negative PDMS mold. By analyzing the quality of negative molds, the spin-coated mold with 5% PAA had a better overall quality. Therefore, applying spin coating on the negative PDMS mold to fabricate the positive mold was a better approach. The schematic of the positive mold fabrication is shown in Figure 2.14.

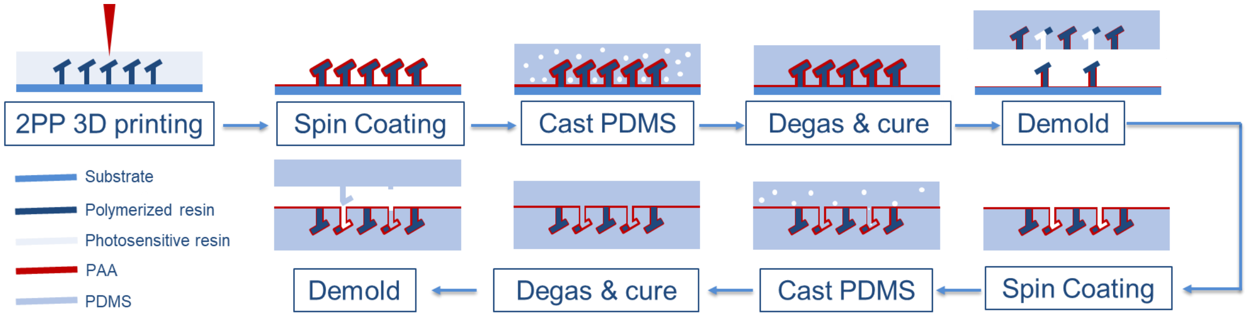

Figure 2.14 Schematic of the positive mold fabrication with defects.

The negative PDMS mold for the multi-design structure panel was spin-coated with 5% PAA. Furthermore, PDMS was poured on top of the negative PDMS mold to replicate the positive mold. Nonetheless, outlines of the design were observed, and the multi-design structure panel was not fully replicated.

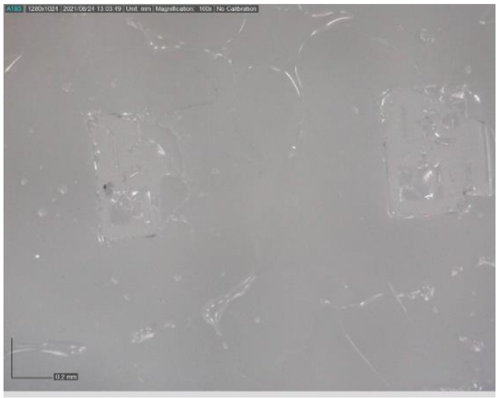

Figure 2.15 Replicated positive multi-design structure panel PDMS mold with no microstructures reserved.

The negative PDMS mold's surface containing microstructures was covered by 5% PAA and degassed at 700 mmHg for 120 seconds. The negative PDMS mold was then spin-coated at 2000 RPM for 60 seconds. To replicate the positive mold, PDMS was poured on top of the negative PDMS mold. The replicated positive mold was demolded, though not all the gecko setae could be demolded from the negative mold successfully. Some gecko setae structures were utterly stuck in the negative PDMS mold, and some gecko setae had broken tips.

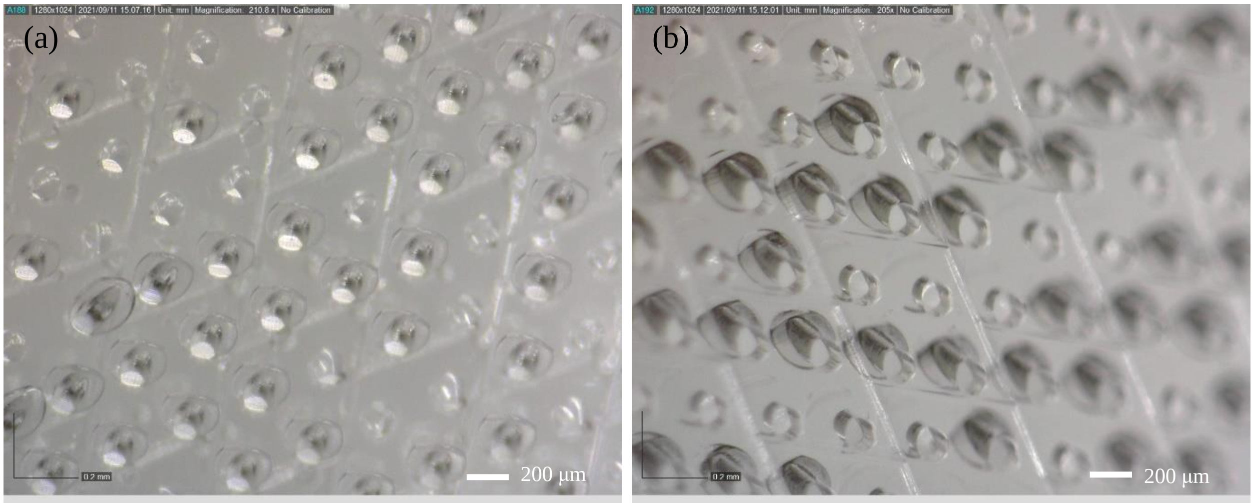

Figure 2.16 (a) Angled view of replicated positive gecko setae array with defects and (b) angled view of the pilled off negative PDMS mold with trapped microstructures.

Comparing the negative mold and positive mold in Figure 2.16, they all have missing structures, and the tilted panels on the molds have broken tips. Therefore, the microstructure mold fabrication failures were more likely to have happened before the first demolding process, which is the negative mold demolding. The broken tips on the microstructures might be caused by the stress concentration at the sharp edge boundary between the tilted panel and the tilted pillar. Meanwhile, having stuck gecko setae in the negative mold might be due to incorrect PDMS curing and demolding processes. The factors that can affect the curing process are temperature and curing time. According to the removal and stripping process from Nanoscribe, the 2PP 3D printed objects will be detached from the substrate due to the differences in their coefficients of expansion. The suggested temperature for stripping is about 100 °C [45]. Therefore, the PDMS curing temperature, which was 90 °C, was too high and caused the printed microstructures to detach from the substrate and get stuck in the negative mold.

2.5 Finalized Fabrication Procedure

The quality of the negative and positive molds was significantly increased by modifying the design of the artificial gecko seta and the fabrication procedure. First, the overhanging tilted panel was changed to connect to the tilted pillar smoothly, and the edge fillet with a radius of 2 μm was added to the tilted panel’s tip, as shown in Figure 2.17.

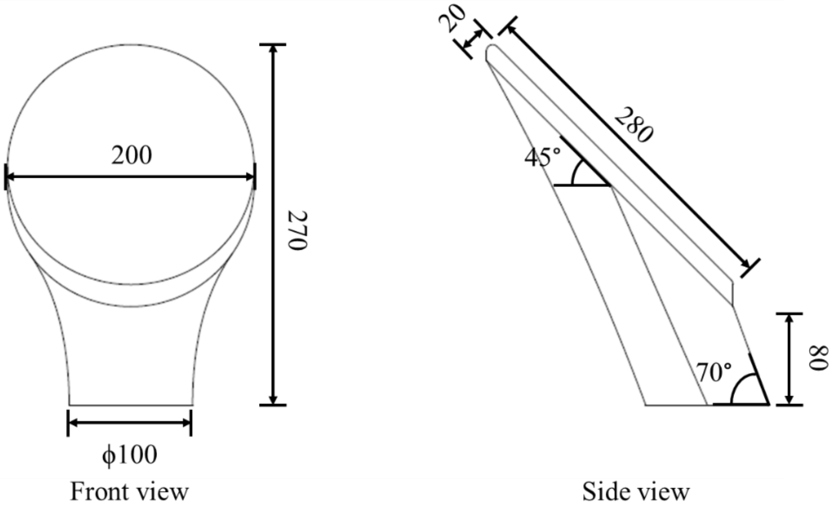

Figure 2.17 Modified tilted mushroom-shaped design (unit: µm).

Based on the product information for Sylgard 184, the curing time for the 10: 1 mixing ratio (base and curing agent) at room temperature is about 24 hours [46]. As Figure 2.18 shows, after the master mold was printed and spin-coated, mixed Sylgard 184 was cast on the master mold. The uncured PDMS was degassed in a vacuum chamber at 700 mmHg, then cured at room temperature for 36 hours. The extension for curing time from 24 hours to 36 hours at room temperature was due to non-fully cured PDMS with sticky exposed surfaces at 24 hours.

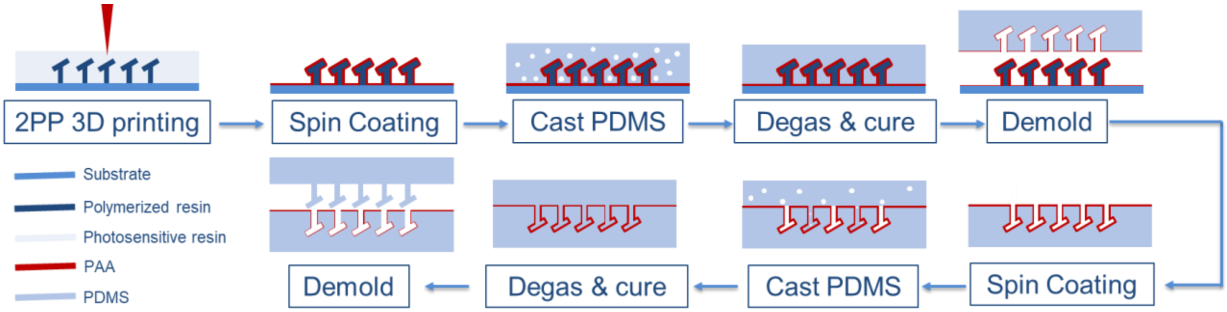

Figure 2.18 Schematic of the finalized negative and positive molds fabrication.

The issues of stuck gecko setae and having broken tips in the negative mold have been resolved, as shown in Figure 2.19 (a). The printed gecko setae were fully detached from the negative mold, and the shape of the gecko setae can be determined clearly in the negative mold. By cutting the negative mold along the tilted direction of the gecko seta, the cross-section view was observed in Figure 2.19 (b). The empty slots in the negative mold are identical to the modified, mushroom-shaped design.

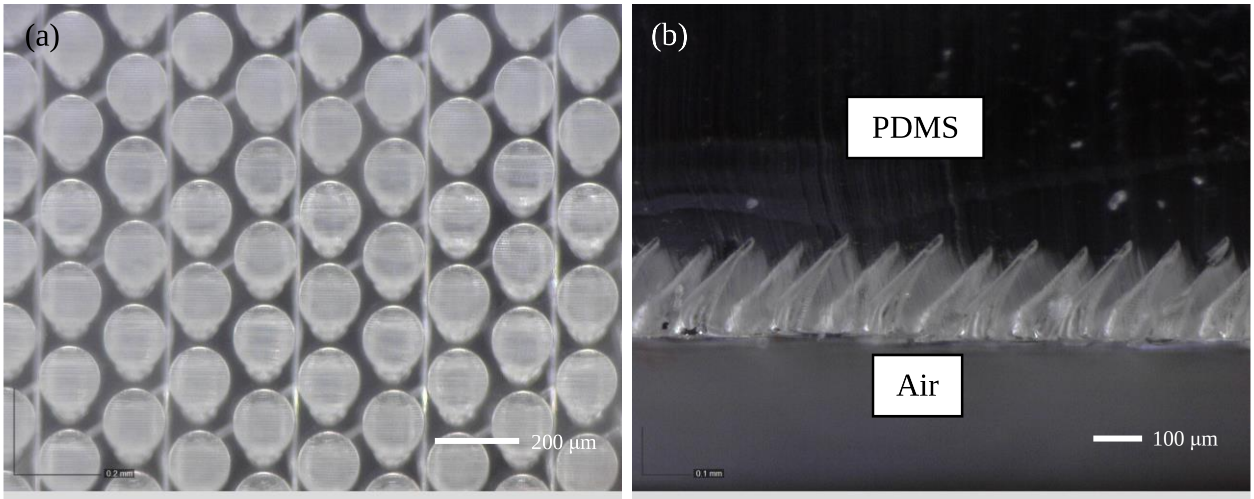

Figure 2.19 Negative mold of Modified tilted mushroom-shaped design. (a) Top view. (b) Cross-section view.

Once the negative mold was fabricated without defect, the positive mold was also fabricated based on the adjusted process, which was changing the curing temperature to room temperature. As Figure 2.20 (a) shows, the microstructures of the replicated positive mold had no broken tips or missing setae. Meanwhile, the gecko seta had uniform height, diameter, and spacing, as shown in Figure 2.20 (b).

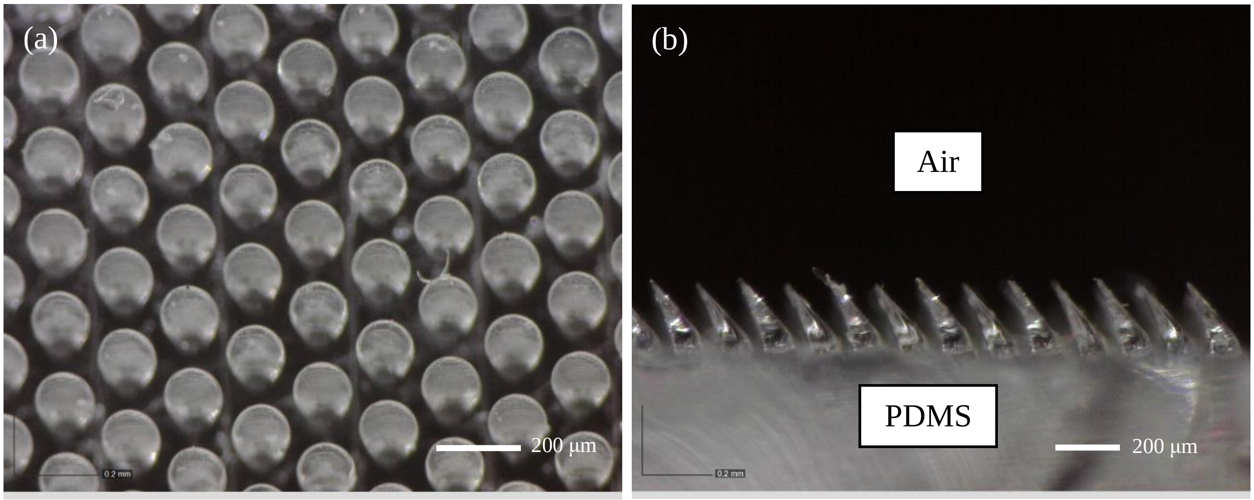

Figure 2.20 Positive mold of Modified tilted mushroom-shaped design. (a) Top view. (b) Cross-section view.

The medicated mold fabrication process had successfully produced a negative mold and a positive mold for artificial setae without any defects. This fabrication process has the advantages of easy design prototyping and scalable producing by comparing with micromachining. For micromachining, a microtome blade needed to be designed and fabricated to cut the wax mold to make the microstructures. The quality of the wedge microstructures fabricated by micromachining highly depended on the blade's dimensions and movement. To produce the wedge-shaped microstructures with a new design, the dimensions and movement of the microtome blade need to be modified. However, the design of the microstructures that were fabricated by 2PP 3D printing can be easily changed by modifying the CAD model and loading the CAD file to the 3D printing software. Once the master mold is fabricated, multiple negative molds can be produced by casting PDMS onto the master mold and curing it. By combining the negative molds in an array and casting PDMS onto the negative molds, a positive mold with a larger area of microstructures can be fabricated.

3 Performance of Dry Adhesion

Multiple designs with various shapes, heights, and scales were fabricated with the 2PP 3D printing and molding process, and the adhesion of each design was tested by a load cell. The effects of the shapes, heights, and scales on adhesive performance could be observed.

3.1 Tested Microstructures Designs

The tested microstructures designs were tilted mushroom-shaped and wedge-shaped. Two tilted mushroom-shaped microstructures were designed to observe the effect of alternating heights of artificial setae on the adhesion performance. The isometric view of the tilted mushroom-shaped design with the same height (SH) and the tilted mushroom-shaped design with a different height (DH) are shown in Figure 3.1(a) and (b). The dimension of the long artificial seta was shown in Figure 2.17, and the short artificial seta was designed by trimming 50 μm of height from the root of the long artificial seta.

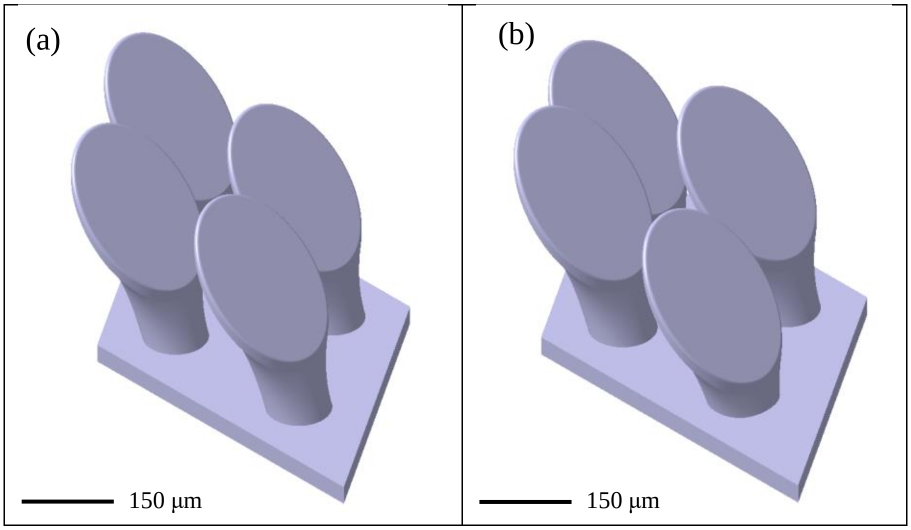

Figure 3.1 The isometric view of (a) SH (b) DH in CATIA.

Meanwhile, four miniaturized microstructures were designed to discover the adhesive performance on a smaller scale which were a miniature tilted mushroom-shaped design with same height (MS), a miniature tilted mushroom-shaped design with a different height (MD), a miniature wedge-shaped design with same height (WS), and miniature wedge-shaped design with a different height (WD). The isometric views of all the miniature designs are shown in Figure 3.2.

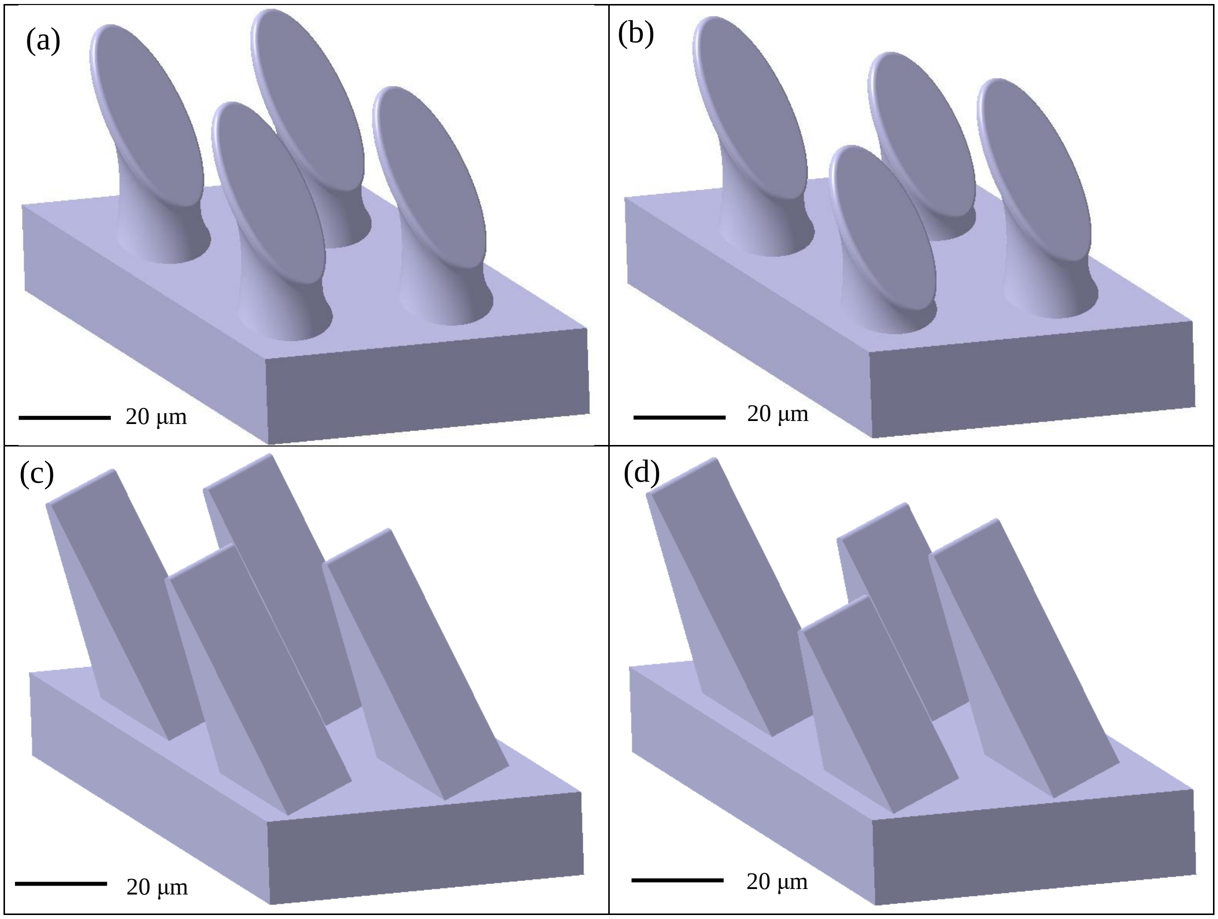

Figure 3.2 Isometric view of (a) MS (b) MD (c) WS, and (d) WD in CATIA.

With a comprehensive consideration of the printing time and quality of the master molds and the difficulty of the demolding process, the heights of the artificial seta in MS and WS were designed to be 40 μm, which was within the range of height in Table 1.2 and 1.3. The diameter of the root of MS and WS width were set to 20 μm to let the aspect ratio be 2. Referring to the designs in Table 1.2, the panel's tilted angle and the pillars' tilted angle were set to 45° and 70°, respectively.

The curvatures of the pillar in MS were not the major design parameters, and the main purpose of the curvatures is to reduce the material in the pillar, which can shorten the printing time and lower the strength of the pillar. By lowering the strength of the pillar, the artificial seta could be bent easier, but it had a higher potential to be damaged during the demolding process. The height of the connection of the tilted panel and the pillar was set to 10 μm, referring to the ratio of the height transition point to the overall height design in Figure 2.17. The dimensions of MS and WS are shown in Figure 3.3.

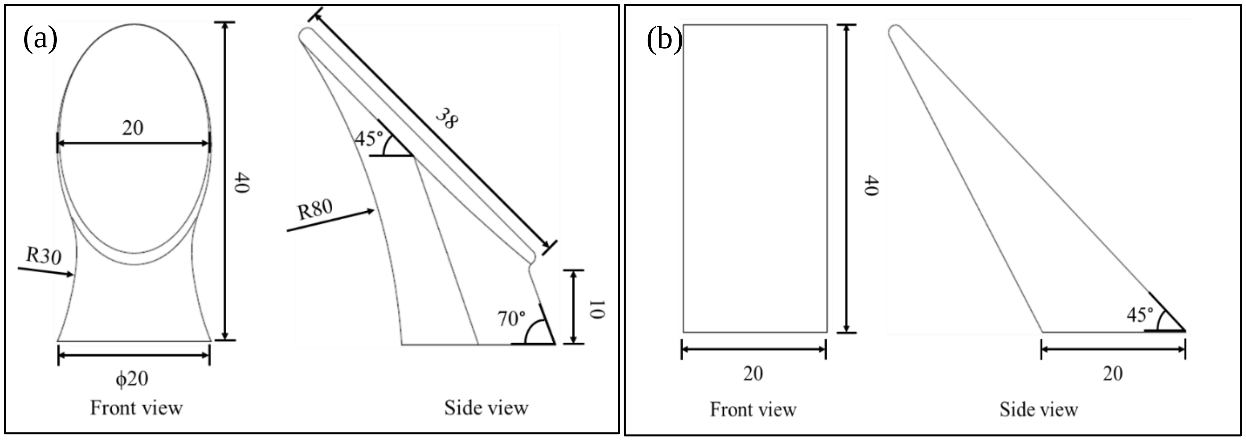

Figure 3.3 Dimensions of the artificial seta in (a) MS and (b) WS (unit: μm).

The longer artificial setae of MD and WD had the same dimension as the artificial setae in MD and WD, respectively. The overall heights of the shorter artificial setae of MD and WD were 10 μm lower than the longer artificial setae. The dimension of the shorter artificial seta in MD and WD are shown in Figure 3.4. The tilted angles, width, diameters, and curvatures remained unchanged.

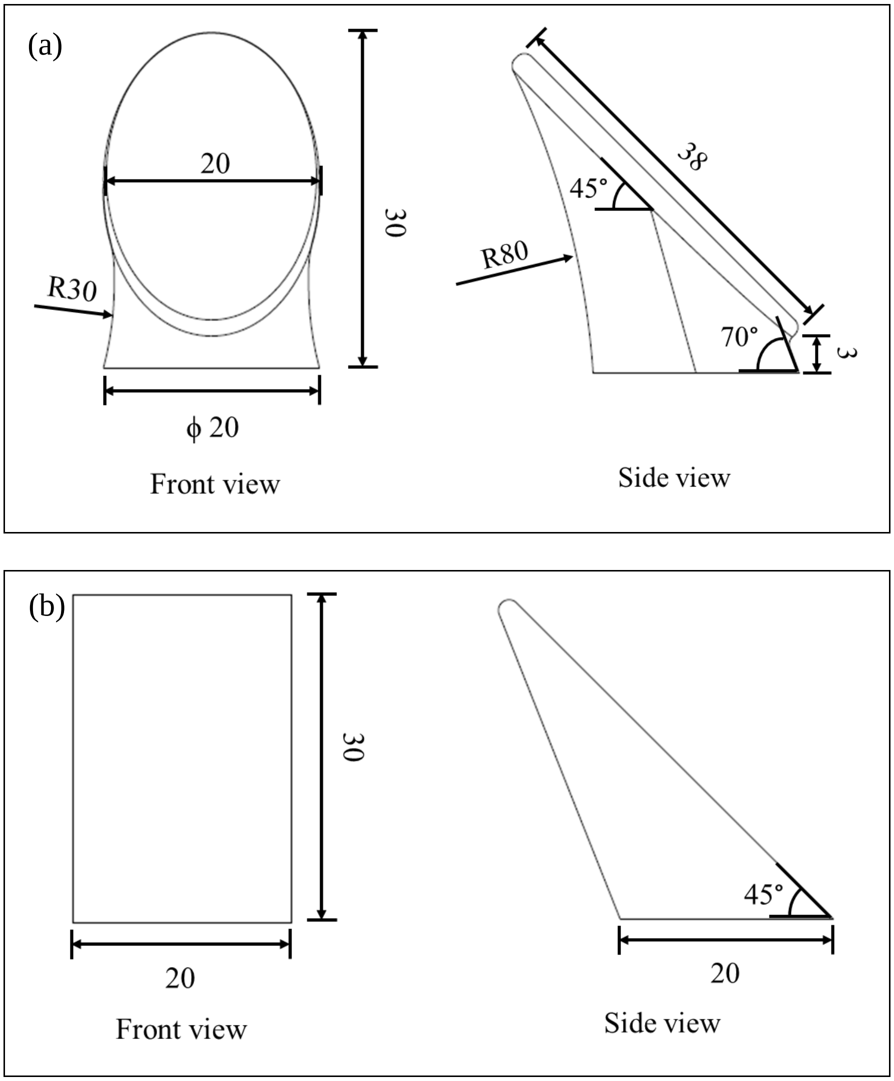

Figure 3.4 Dimensions of the artificial seta in (a) MD and (b) WD (unit: μm).

3.2 Roughness of Tested Surface

The tested surfaces were glass (Globe, USA), silicon wafer (UniversityWafer, USA), and aluminum plate. Their surface roughness was also determined. The typical root-mean-square (RMS) roughness of the laboratory glass surface ranged from about 2 to 10, equivalent to a roughness value Ra of 0.05 to 0.2 μm [47]. The surface roughness of the aluminum and the silicon wafer was measured with a 3D profilometer, The Profilm3D (Filmetrics, USA), and the surfaces were shown in Figure 3.5. The roughness values Ra of the aluminum plate and the silicon wafer were 0.557 µm and 0.016 µm, respectively.

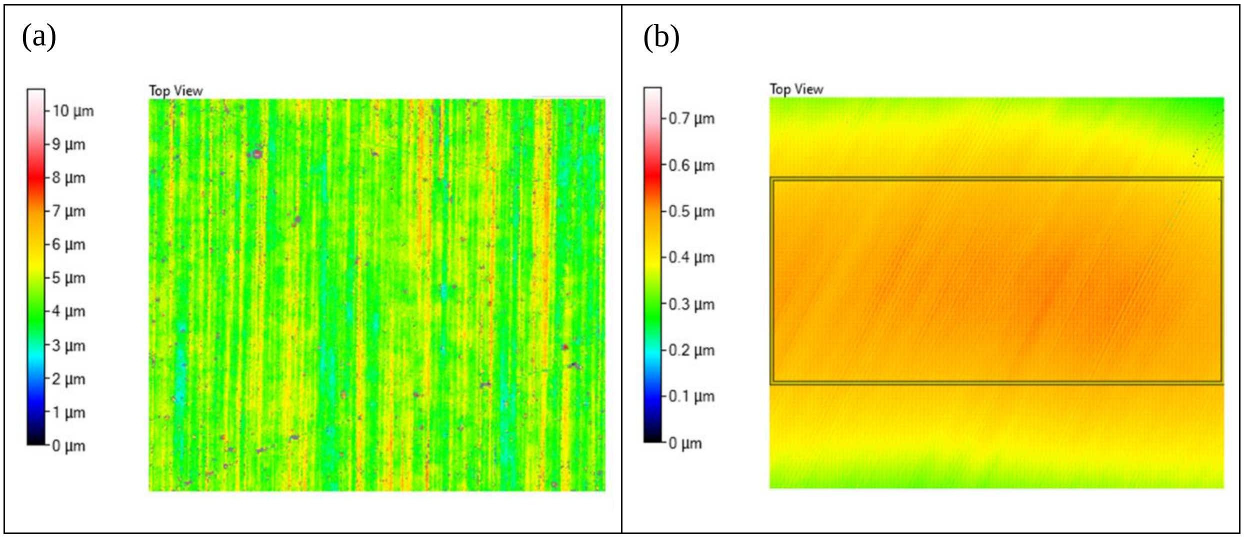

Figure 3.5 Surface of (a) aluminum plate and (b) silicon wafer scanned by a 3D profilometer.

3.3 Equipment Setup

To measure the adhesion provided by the gecko setae microstructures, the microstructures needed to be compressed onto the attached surface to ensure the micro-pillars were entirely in contact with the surface. Meanwhile, the resolution and accuracy of the load cell should be precise since the adhesion force is minimal. The adhesive performance of the tilted artificial gecko setae microstructures, which were made of PDMS, ranged from 0.3 to 1.8 N/cm^2. For the gecko setae microstructures with the area of 1 cm^2, based on Table 1.2 and Table 1.3, the expected generated adhesion should be 0.3 to 1.8 N. To measure the performance of the dry adhesion, the resolution and the accuracy of the load cell should be precise. A 50 g load cell (FUTEK, USA) was used to test the adhesion of the microstructures. However, the capacity of the load cell was about 0.5 N in tension and compression, which was lower than the maximum adhesion of 1.8 N. By reducing the size of the positive molds to 0.5 cm by 0.5 cm, the expected generated adhesion was decreased to 0.075 to 0.45 N, and the load cell could be used appropriately.

The setup of the adhesion measurement is shown in Figure 3.6. The 50 g load cell was clamped onto a micromanipulator (World Precision Instruments, USA), and a tested surface was attached to the load cell. The load cell, a multimeter (Keysight, USA), and a 12V voltage supplier were connected to a circuit board with two knobs for coarse and fine adjusting the displayed voltage to zero. The tested microstructures sample was placed onto another micromanipulator.

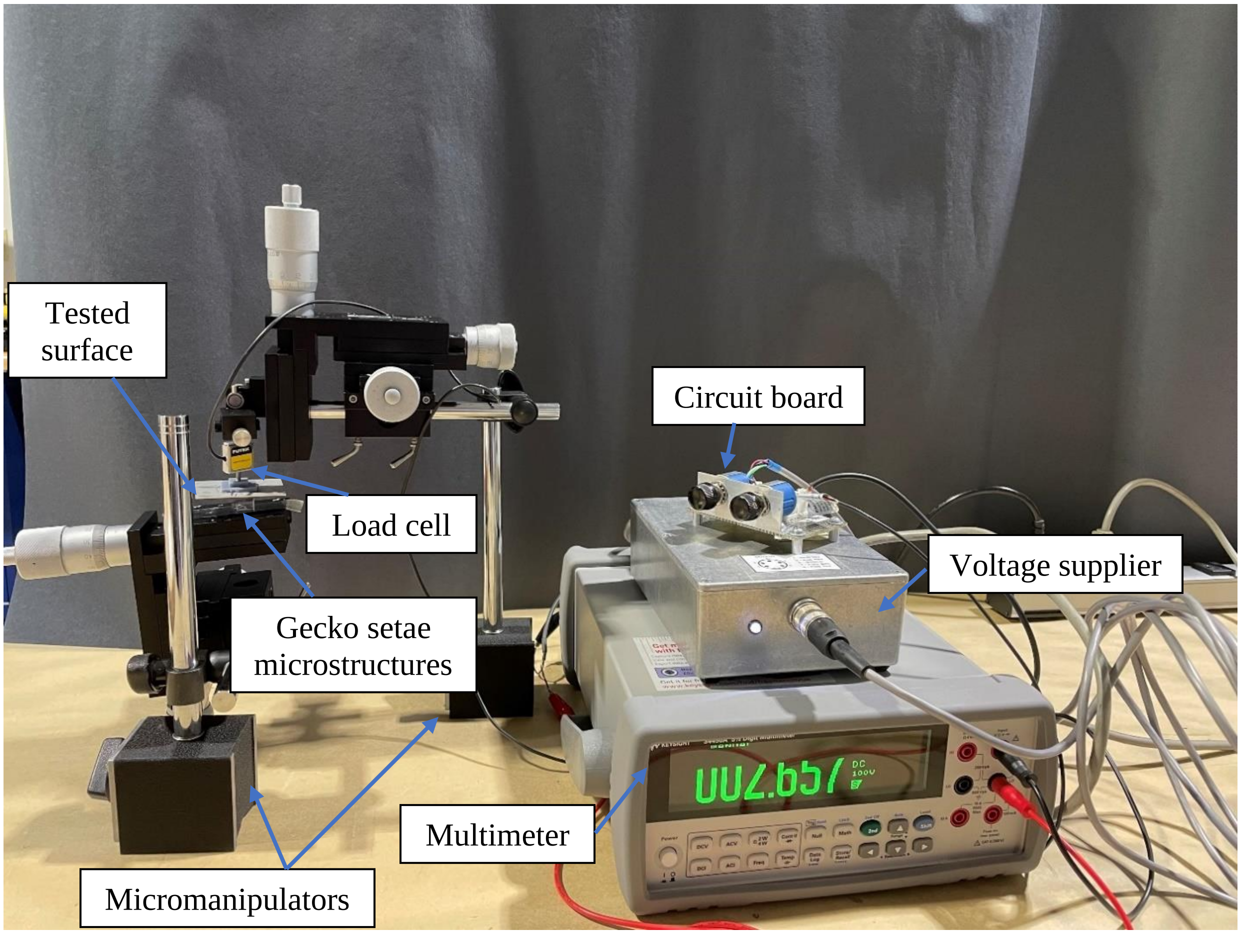

Figure 3.6 Setup of the adhesion measurement

The load cell was calibrated with mass weight, and the correspondent voltages were recorded. The voltage and applied force relationship were obtained by converting the mass to force with a gravitational acceleration of 9.81 m/s2, as Figure 3.7 shown. The slope of the linear regression line for force vs. voltage was 0.0321 N/V.

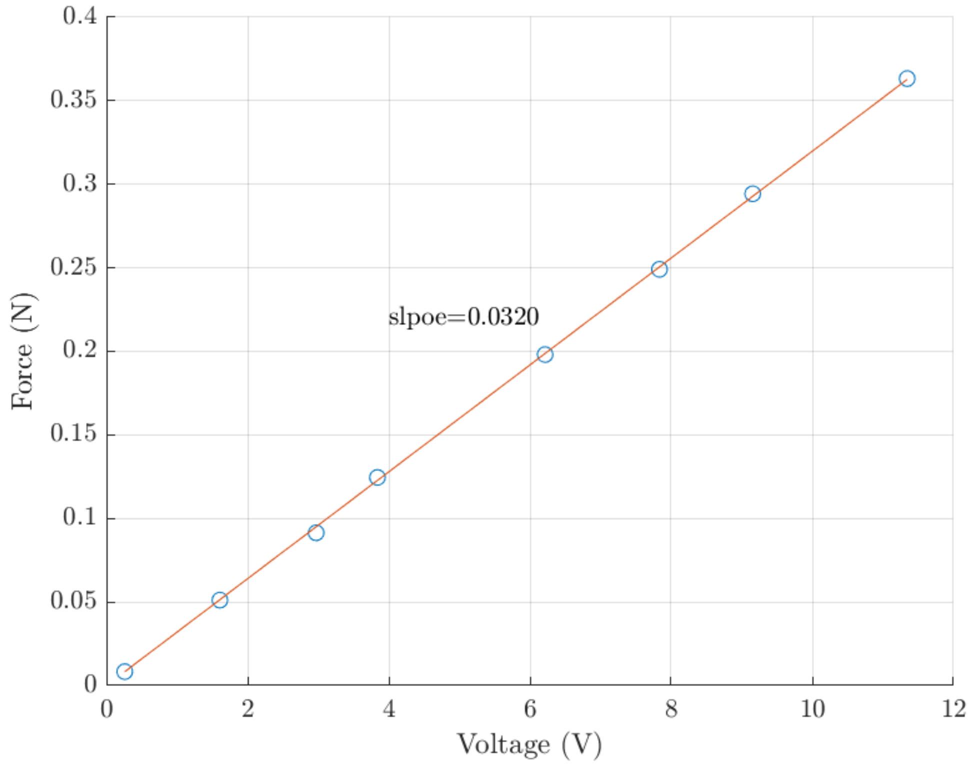

Figure 3.7 Linear regression of 50 g load cell calibration.

Before measuring the dry adhesion force, the tested surface must be hanged by the load cell horizontally. Meanwhile, the top surface of the PDMS sample, which contained the microstructures, was adjusted to be parallel to the tested surface by moving the platform attached to the PDMS sample. Afterward, the voltage showed in the multimeter was adjusted to zero by rotating the knobs on the circuit board. During the test, only the platform of the micromanipulator attached to the PDMS could be moved to raise the PDMS sample to be in contact with the tested surface. Otherwise, if the tested surface were declined to approach the PDMS sample, the measured voltage from the load cell would be changed accordingly, and the measured adhesion would not be correct. In addition, the calculated maximum voltage output of the load cell was about 15.28 V. To ensure that the load cell would not be overloaded and damaged, the magnitude of the limited output voltage was set to 11 V, which would provide an approximate 0.4 margin of safety.

When the test was conducted, the measured voltage should be zero before the tested PDMS sample was in contact with the tested surface. Once the tested surface compressed the PDMS sample, the negative voltage would display on the multimeter. When the compression was released by lowering the PDMS sample, the measured voltage would be increased to zero and even positive values. The measured maximum voltage could be converted to the maximum dry adhesive force with the relationship shown in Figure 3.7. During the test, the measured voltage fluctuated in the degree of millivolt, so the recorded voltage was rounded to two decimal places.

3.4 Result and Analysis

Two tests were conducted: preload versus maximum adhesion and shear distance versus maximum adhesion. The maximum adhesion of the gecko-inspired dry adhesive microstructure was varied depending on the preload. As the preload increased, the maximum adhesion tended to increase and remain stable [44]. As Figure 3.8 shown, the maximum adhesion of the microstructures at various preloads was tested by approaching the tested microstructures to the tested surface to reach the desired preload and then unloading.

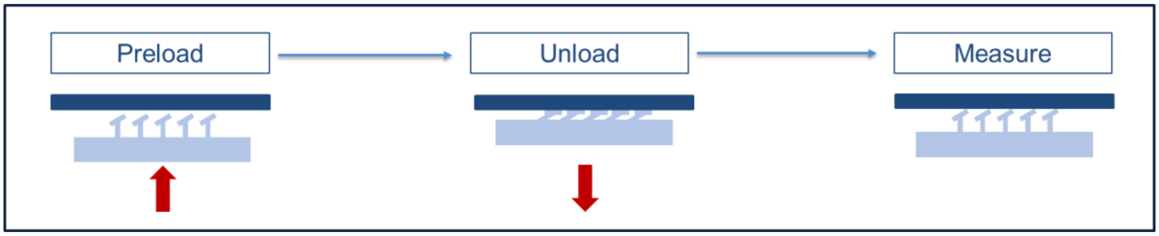

Figure 3.8 Schematic of the preload versus maximum adhesion test.

Similarly, shearing the microstructure once the desired preload was reached and then unloading, the maximum adhesion of the microstructures at various shear distances was measured. As Figure 3.9 shown, positive mold moved toward the left to shear microstructure toward the tilted direction. Every trial test was performed five times, and the mean of each test would be plotted in a figure, and the standard error of the mean would be indicated with the error bar.

Figure 3.9 Schematic of the shear distance versus maximum adhesion test.

3.4.1 Effect of PAA Isolated Layer

During the demolding process between positive mold and negative mold, the PAA isolated layer that spin-coated on the negative mold might adhere to the positive mold. The PAA isolated layer had the potential to lower the adhesive performance and eventually caused the adhesion ~~was too small to~~ to be too small to measure ~~be measured~~ with a 50g load cell. To observe if the PAA isolated layer stuck onto the positive mold and if it would lower the adhesion, a pure PDMS positive mold was fabricated following the process shown in Figure 2.18. The adhesive force of the pure PDMS positive mold was measured under various preload. Afterward, the pure PDMS positive was clean with deionized water and dried with an air blow gun. The adhesive force of cleaned pure PDMS positive was measured and shown in Figure 3.10.

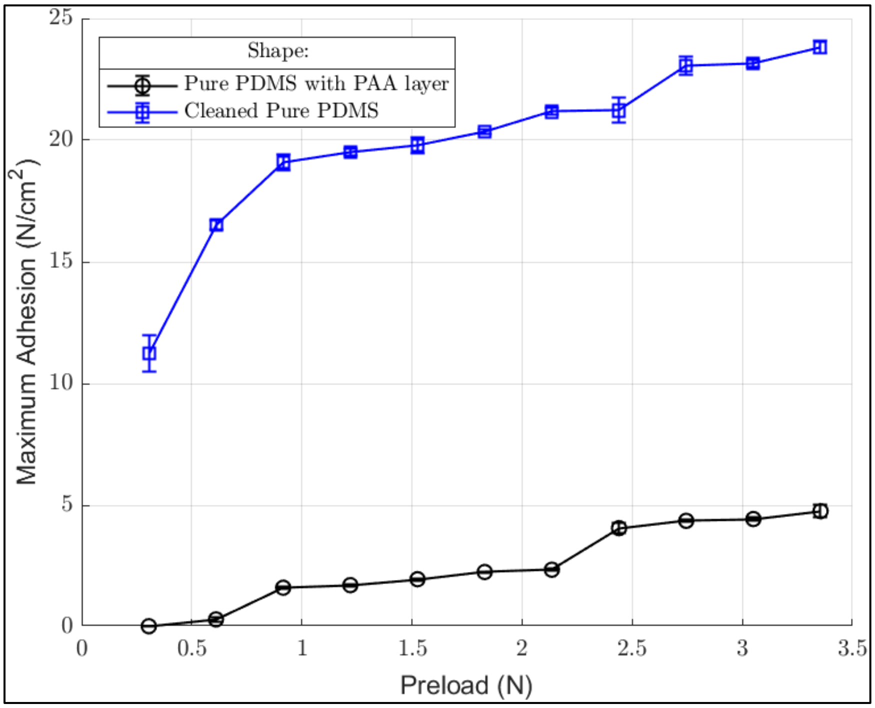

Figure 3.10 Adhesive performance of the uncleaned pure PDMS structure positive mold and the cleaned PDMS positive mold

The maximum adhesion of uncleaned and cleaned pure PDMS structure positive mold increased as the preload increased. The maximum adhesion of the cleaned pure PDMS structure matched the experiment in other studies [48, 49]. The maximum adhesion at zero preload was not measured because adhesion did not exist. The cleaned pure PDMS structure positive mold had about four times higher adhesive performance than the uncleaned PDMS positive mold, which was covered by the PAA layer. Therefore, during the demolding process, PAA would adhere to the positive mold and reduce the adhesive performance of the microstructures. The cleaning process was necessary to remove the PAA isolated layer on the positive molds to measure the dry adhesion of the PDMS microstructures accurately.

3.4.2 Adhesion of Pure PDMS Flat Plane on Various Surfaces

Adhesive performance of the cleaned pure PDMS structure on glass, aluminum plate and silicon wafer were shown in Figure 3.11. The pure PDMS structure's maximum adhesion varies on different surfaces, and the pure PDMS structure adheres to the aluminum plate better than the silicon wafer and glass. Based on the measured adhesion and the surface roughness of the tested surfaces, there was no clear evidence to build the relationship between the surface roughness and the adhesion. The peaks of the maximum adhesion of the pure PDMS structure on glass, aluminum plate, and silicon wafer were 23.83 N/cm^2, 25.89 N/cm^2, and 25.77 N/cm^2, respectively. The maximum adhesions of the pure PDMS structure on three tested surfaces tended to increase and remain stable as the preload increased.

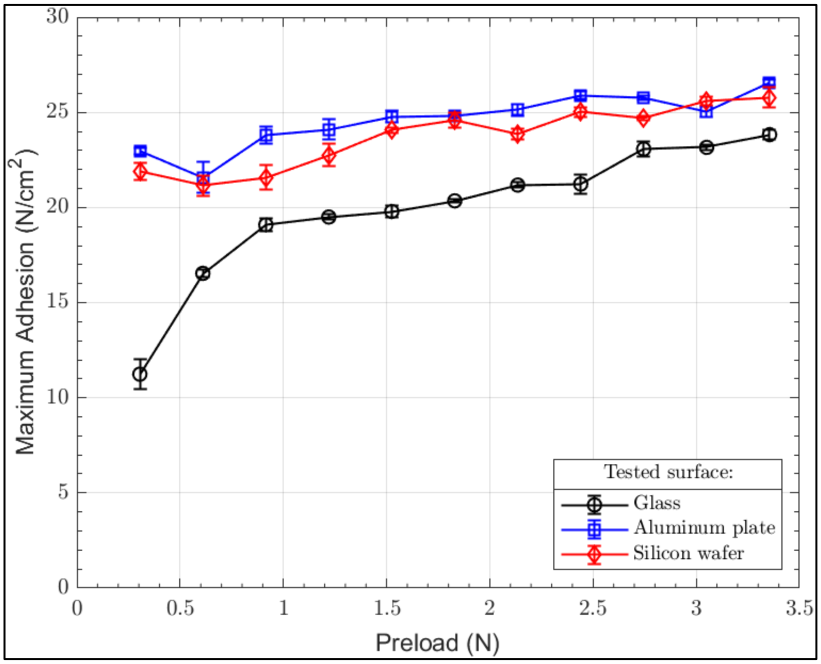

Figure 3.11 Adhesive performance of the cleaned pure PDMS positive mold on glass, aluminum plate and silicon wafer.

3.4.3 Adhesion Comparison for Unifrom Height and Alternating Height Design

The maximum adhesions of SH and DH on glass, aluminum plate, and silicon wafer under various preload stresses were measured, and the results are shown in Figure 3.10. SH had a better adhesive performance on the aluminum plate, while DH adhered to the glass and silicon wafer. By comparing Figure 3.11 and Figure 3.12, the maximum adhesions of PDMS microstructure were significantly lower than pure PDMS structure. SH design had higher adhesion on glass than on silicon wafer, and neglectable adhesion was observed in contact with aluminum plate. The adhesion performance of SH and pure PDMS structure on the tested surfaces conflicted. The adhesion performance of DH design on aluminum plate and silicon wafer were similar, and they were not as good as the adhesive performance on the glass.

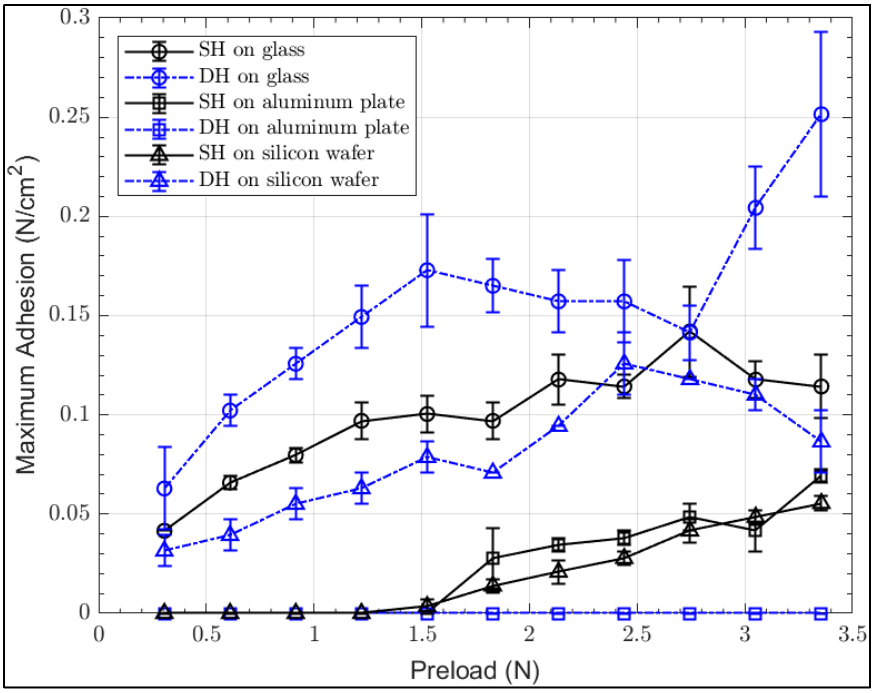

Figure 3.12 Adhesive performance of the SH and DH on glass, aluminum plate and silicon wafer.

DH had better adhesion performance than SH on glass and silicon wafer, and the peak of maximum adhesion of DH was two times higher than the peak of the maximum adhesion of SH. However, SH had better adhesion performance than DH on the aluminum plate, as the adhesion of DH was not measurable. By only applying preload, the maximum adhesions of the tested positive molds tended to increase as the preload increased. Therefore, the preload applied to the maximum adhesion versus shear distance test would be set to 3.4 N.

During the shear distance versus maximum adhesion test, 3.4 N of preload was applied onto the positive mold and sheared to the desired distance. The maximum adhesion was measured while the positive mold was moved away from the tested surface. The limit of the shear distance was set to 600 μm, which was about two times the height of the artificial seta in SH. As Figure 3.13 shown, the PDMS positive mold was under and in contact with the glass surface. When 3.4 N preload was applied, the microstructures were fully bent. As the positive mold shifted toward the right, the positive mold was tilted due to the shear force. The microstructures at the right edge of the positive mold experienced higher compression force than the microstructures at the left edge of the positive mold.

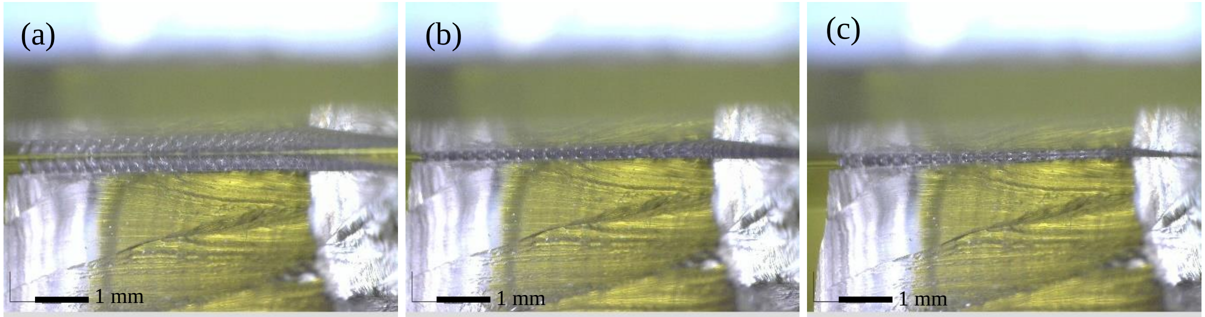

Figure 3.13 Schematic of SH positive mold shear on glass. (a) Positive mold in contact with glass surface with zero preload. (b) 3.4 N preload was applied to the positive mold. (c) The positive mold moved toward right for 300 μm to shear the microstructures.

As Figure 3.14 shown, SH had better adhesive performance than DH while shear was applied. The peaks of the maximum adhesion versus shear distance curve for SH on glass, aluminum plate, and silicon wafer were 1.27 N/cm^2, 1.48 N/cm^{2,} and 1.18 N/cm^2, respectively. The adhesions of DH on different tested surfaces were too small to be measured with the 50g load cell, so the effect of the microstructure design with alternating heights on other surfaces could not be investigated. Regarding adhesion, SH design performed significantly better than DH design on all tested surfaces. As a result, the design of the alternating heights of artificial setae could not improve the adhesion performance on the surface, with the surface roughness value Ra ranging from 0.016 µm to 0.557 µm.

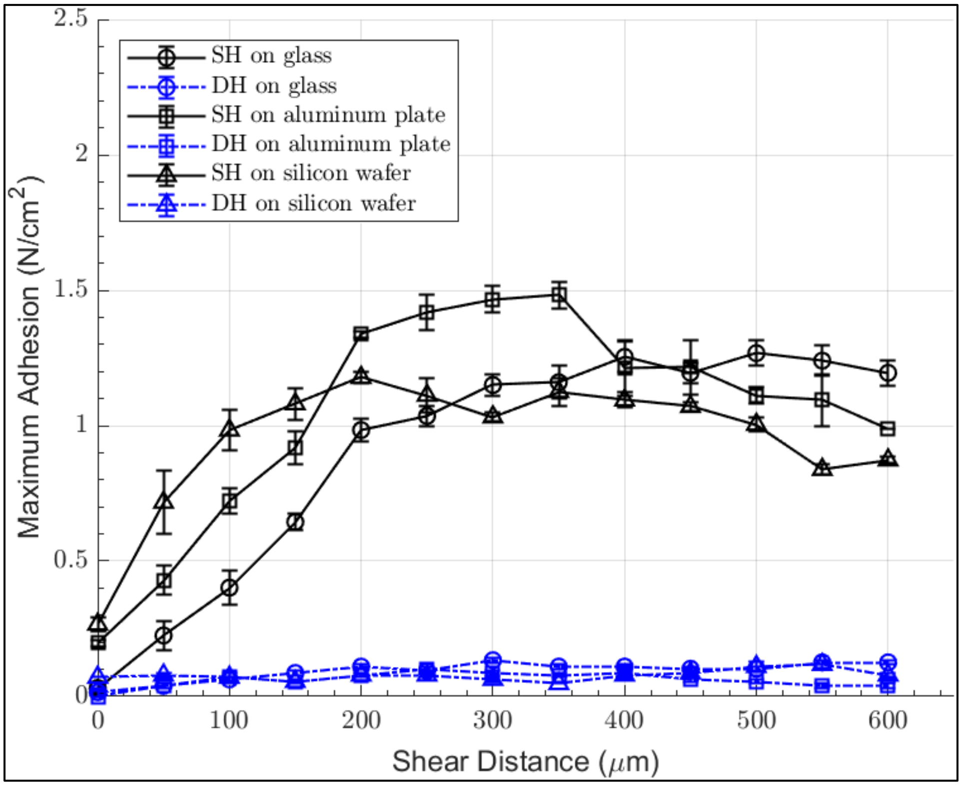

Figure 3.14 Adhesive performance of the SH and DH on glass, aluminum plate and silicon wafer with shear.

3.4.4 Adhesion Comparison for Scale Difference and Shape Difference

The maximum adhesions of MS, MD, WS, and WD on glass, aluminum plate, and silicon wafer under various preload stress were measured, but they were too small to be measured with a 50g load cell, and the measured voltages were zero. The shear distance versus maximum adhesion test was conducted by applying 3.4 N/cm^2 of preload and shearing from 0 μm to 80 μm with a 10 μm increment. The result of the maximum adhesions of four tested miniature designs onto three tested surfaces was shown in Figure 3.15, Figure 3.16, and Figure 3.17.

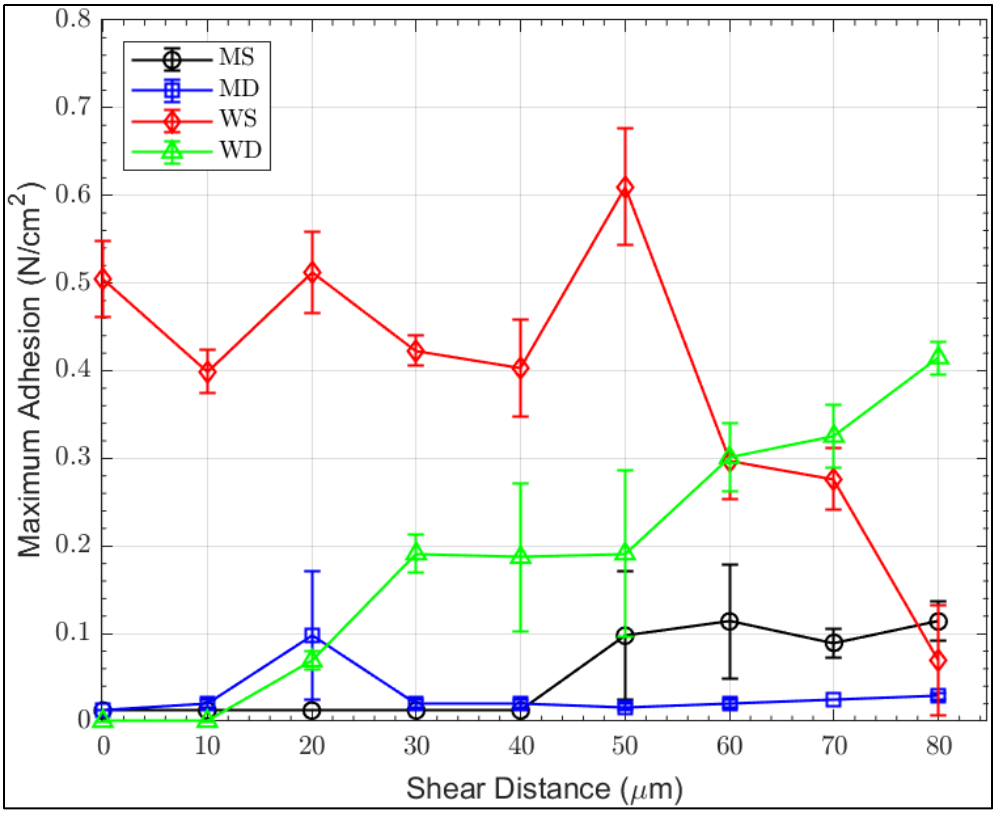

Figure 3.15 Adhesive performance of the MS, MD, WS and WD on glass

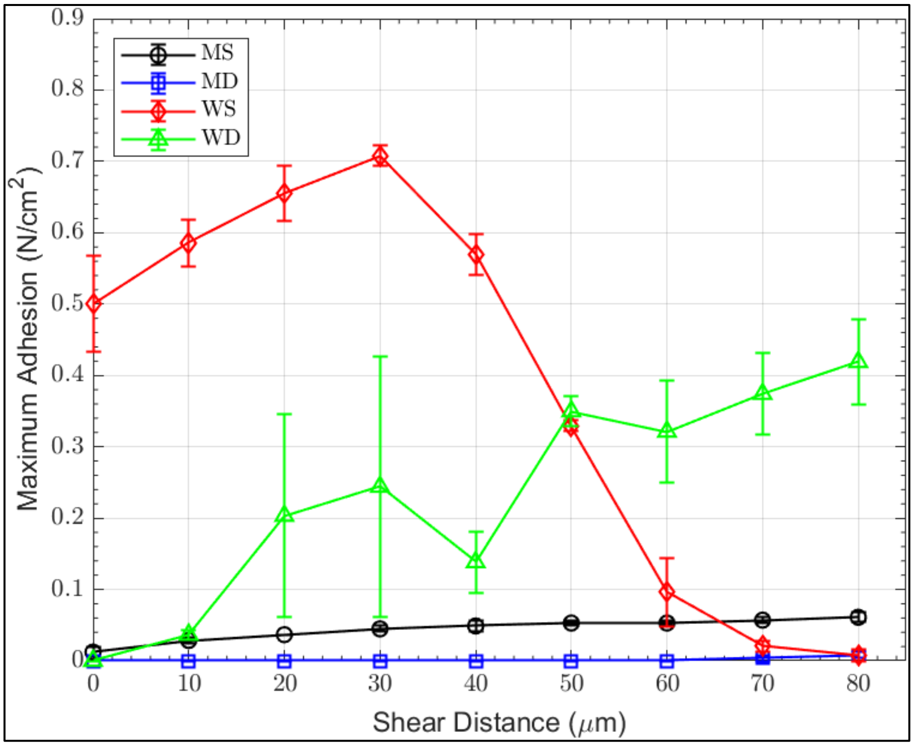

Figure 3.16 Adhesive performance of the MS, MD, WS and WD on the aluminum plate

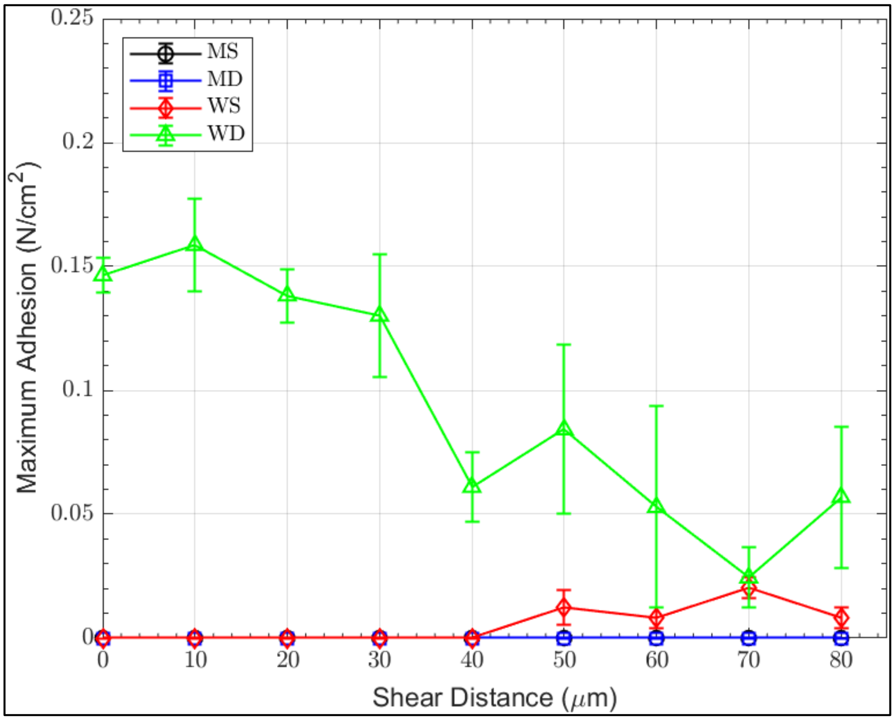

Figure 3.17 Adhesive performance of the MS, MD, WS and WD on silicon wafer

By comparing Figure 3.14 with Figure 3.15, Figure 3.16, and Figure 3.17, the overall adhesion performances of the miniature microstructures were poorer than the SH. The tilted mushroom-shaped design lost about 50% adhesion on glass and aluminum plates and lost approximately 98% of adhesion on a silicon wafer. In terms of the shape, the wedge-shaped design had greater adhesive performance than the tilted mushroom-shaped design. In particular, miniature wedge-shaped designs with the same height adhere to the glass and aluminum plate while the shear distance was less and equal to 40 μm. As the shear distance became larger than the 60 μm, the wedge-shaped design with different heights was better than the others. The microstructures with the alternating heights of artificial setae were ineffective in adhesion performance because the aspect ratio of the shortened setae was less than 2.

The low adhesion performance of the miniature microstructures might be caused by the defection of the tested positive molds. To investigate the integrity of microstructures on the positive molds, Scanning Electron Microscopy (SEM) was used to scan across the surfaces of the cross-section of the cut positive molds. As Figure 3.18 shown, defected artificial gecko setae were found in all the miniature microstructures. Broken tips, missing pillars, and trapped particles were ubiquitous.

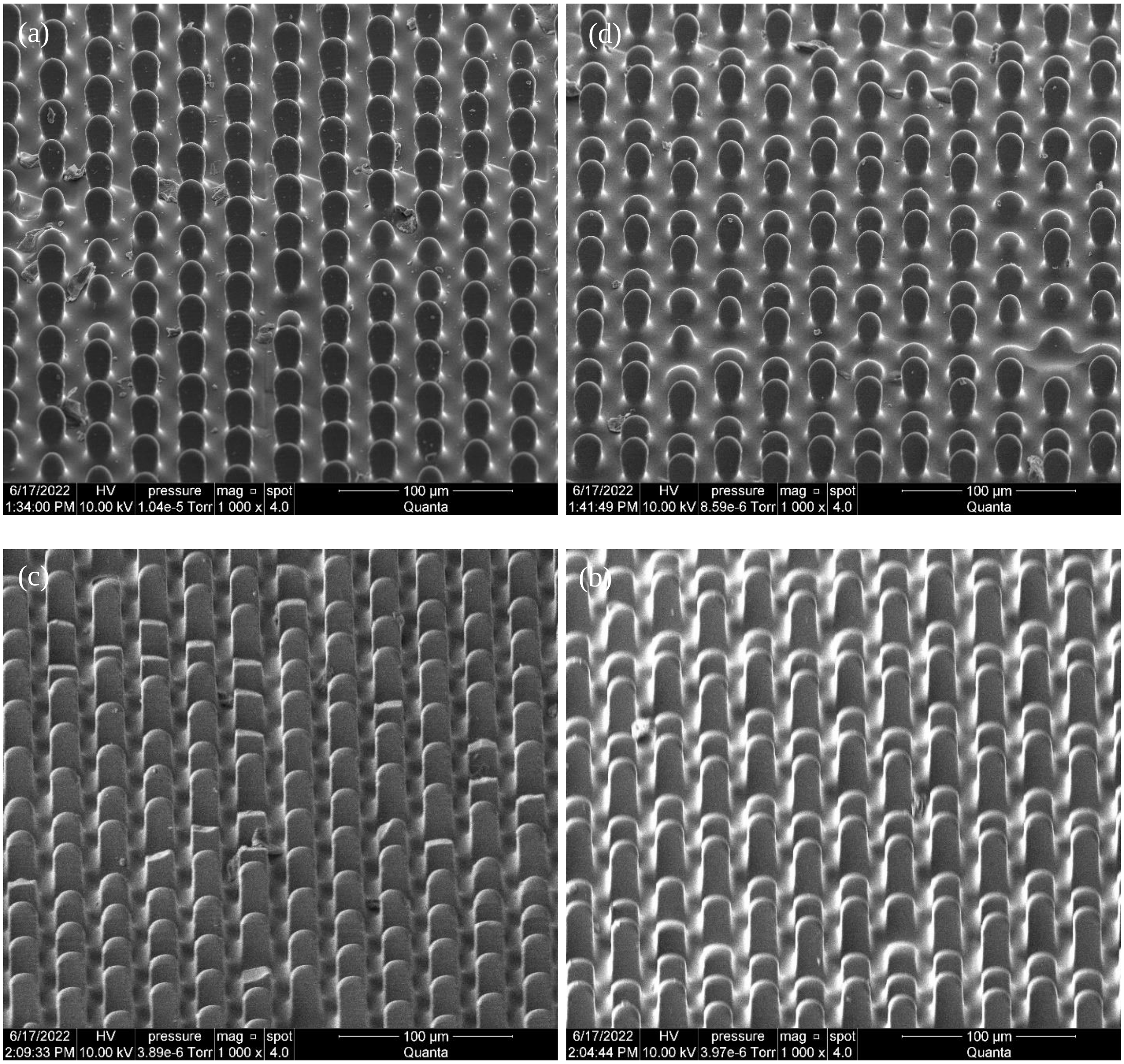

Figure 3.18 Inclined front views of PDMS miniature microstructures. (a) MS design (b) MD design (c) WS design and (d) WD design.

The bumps are shown in Figure 3.18 (a) and (b) were caused by the non-completed filled gaps while casting PDMS onto the negative molds. Air bubbles were trapped in the gaps of the nagative mold and prevented PDMS fulfill the gaps. The broken tips are shown in Figure 3.18 (c) might be caused by the flaws of the PAA isolated layer. The tips of the wedge-shaped microstructures adhered to the nagetive mold where the gaps were not covered by the PAA isolated layer and fractured during the demolding process. Trapped particles were discovered in all the miniature microstructures, which was not avoidable in common laboratory environmental conditions.

By comparing Figure 3.19 (a) and (c), the final product of the miniature tilted mushroom-shaped micropillar was thicker and straighter than the wedge-shaped design. These differences in the microstructures led to the tilted mushroom-shaped micropillar having higher bending resistance and easier to recover when the structures were bent. Meanwhile, the shortened artificial gecko setae were too short in Figure 3.19 (b) and (d) and would have a less effective contact area than the long artificial gecko setae during shearing.

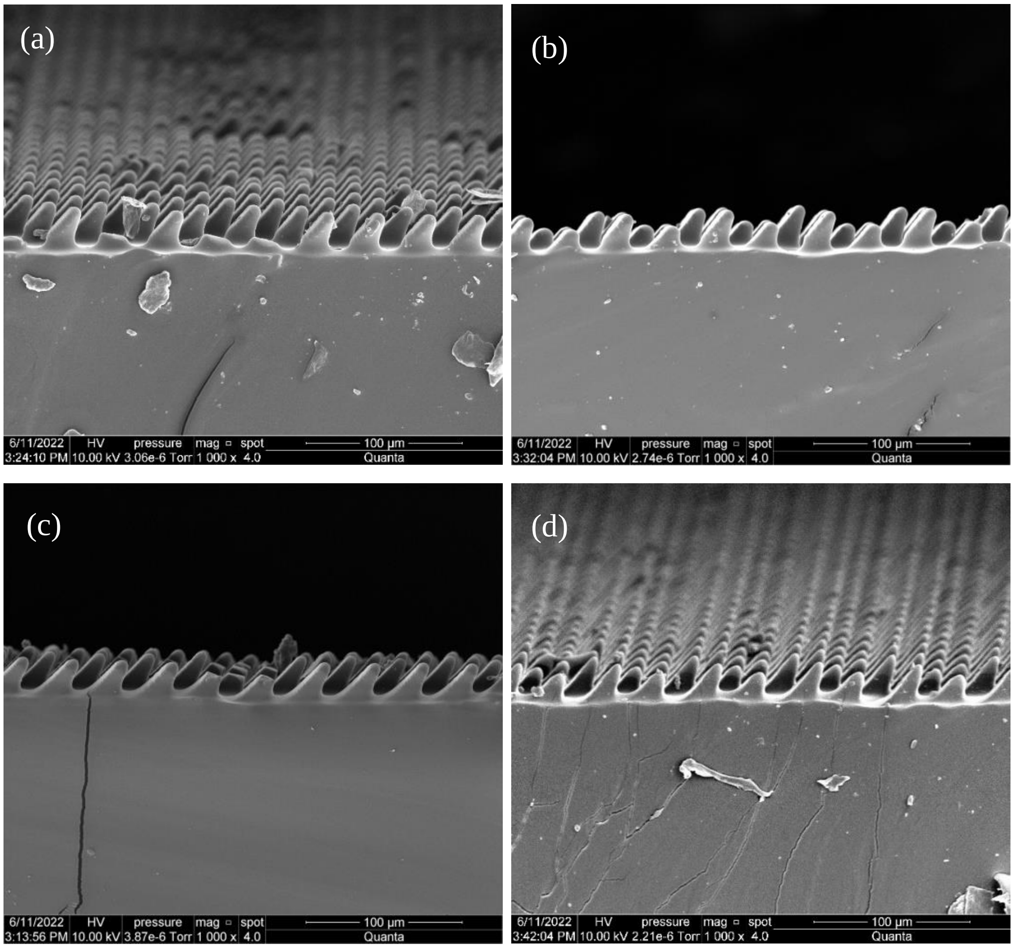

Figure 3.19 Cross-section of PDMS miniature microstructures. (a) MS design (b) MD design (c) WS design and (d) WD design.

After the miniature microstructures experienced multiple times of 3.4 N preload force and 80 μm shear movement, the microstructures were scanned with SEM to investigate the condition of the micro-pillars. As Figure 3.20 (a) shows, the micropillars on the MS design are laid down toward the tilted direction of the micro-pillars and cannot cover their original shape. Since PDMS elastomer had recoverability under compression, the cause should be the adhesion between the back surface of the tilted mushroom-shaped seta and the base. The unrecoverable micro-pillars would lower the adhesive performance of the microstructure due to the loss of effective contacted area. Because the adhered micro-pillars tended to lay toward the gaps between the columns of micro-pillars, this issue could be resolved by reducing the spacing distance between the columns and having adjacent microstructures to hinder the micropillars from sticking to the base. Figure 3.20 (b) shows cracks forming on the wedge-shaped microstructures. The cracks were allocated at the center of the tilted panels across the width direction. The applied preload force and shear distance should be decreased to avoid material failures.

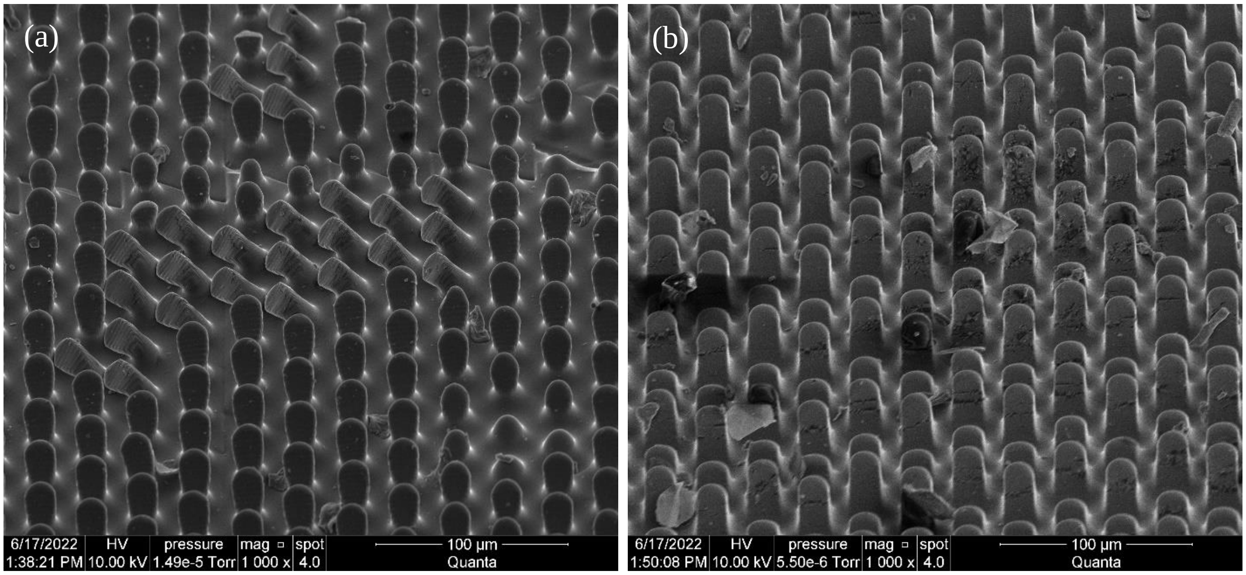

Figure 3.20 (a) Unrecoverable micro-pillars on the MS design when preload and shear were applied. (b) Propagated cracks on the WD design when preload and shear were applied.

3.4.5 Numerical analysis

Numerical analysis was performed to obtain the stress and theoretical effective contacted area of the miniature microstructures to a flat surface. 3D MS and MD design models were imported to COMSOL and modeled as shown in Figure 3.21 (a) and (b). The tilted mushroom-shaped artificial setae stood on the cuboid base with a thickness of 30 μm, and the material of the artificial setae and base material was PDMS, which was a built-in material in COMSOL. The behavior of PDMS was represented by the fifth-order Mooney-Rivlin parameters [44]. The cuboid block above the artificial setae was a flat aluminum plate. To reduce the simulation's computational time, as Figure 3.21 shown, the WS and WD designs were analyzed in 2D since the wedge-shaped design had uniform thickness.

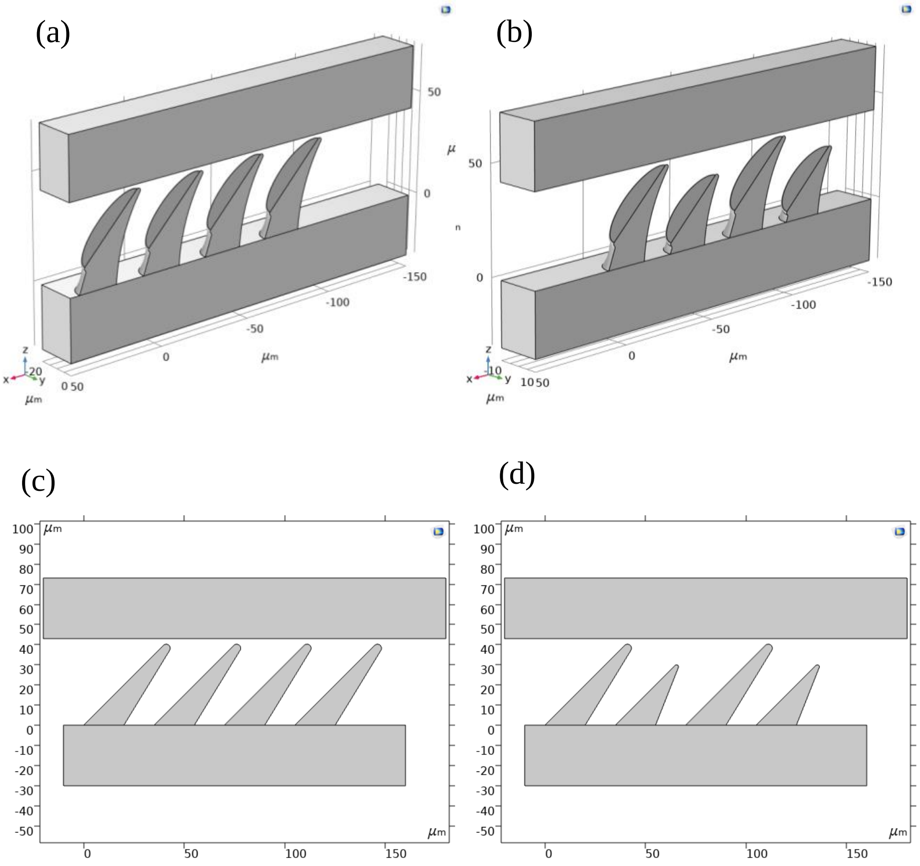

Figure 3.21 COMSOL models of (a) MS and (b) MD in 3D. COMSOL models of (c) WS and (d) WD in 2D.

MS design was model in COMSOL Multiphysics 6.0 with Structural Mechanics module and Nonlinear Structural Materials Modules. The CAD model of a single artificial seta in CATIA was saved as an STL file and imported to COMSOL, ~~and~~ where it was cut in~~to~~ half by a block with Difference. Two blocks with 200 µm of width, 20 µm of depth, and 30 µm of height were built below and above the half seta, respectively. An array of ~~4~~ four half seta was built along negative x-direction with a spacing of 35 µm. The half setae and the lower block were set to be a Union, and the upper block was set to form an assembly. Default mesh with finer element size was used. The final geometry is shown in Figure 3.22.

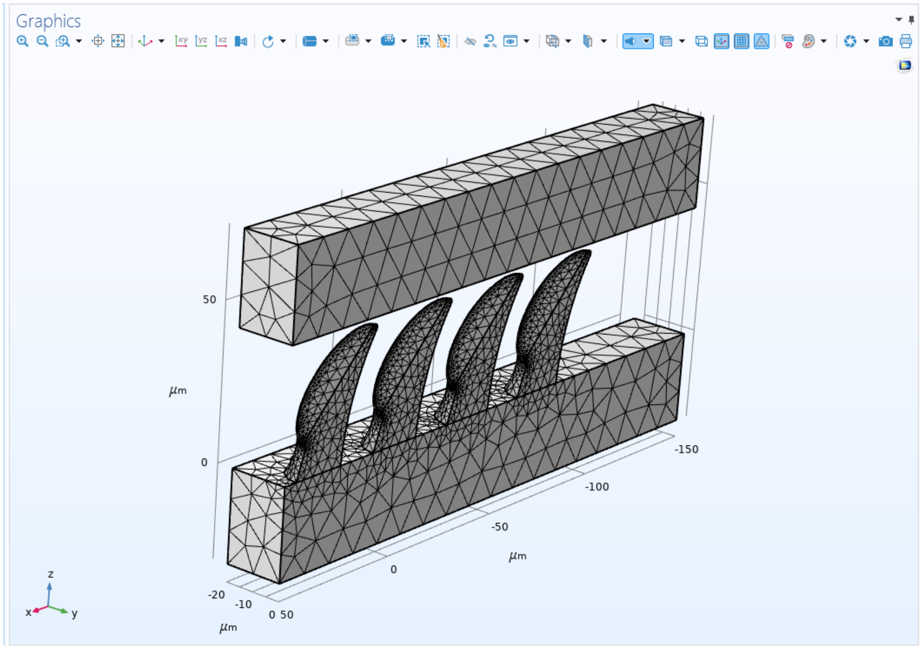

Figure 3.22 Geometry model of MS with mesh in COMSOL.

The upper block was assigned aluminum, with Young’s modulus of 70 Gpa, Poisson’s ratio of 0.33, and a density of 2700 kg/m^3. The half setae array and the lower block were assigned to be aluminum PDMS, with Young’s modulus of 750 kPa, Poisson’s ratio of 0.49, and density of 970 kg/m^3.

To avoid the upper block going through the half setae array, the lower surface of the upper block was defined as the source boundary, and the tilted panels of the half setae were defined as destination boundaries. Meanwhile, contact pairs were defined among the half setae as shown in Figure 3.23.

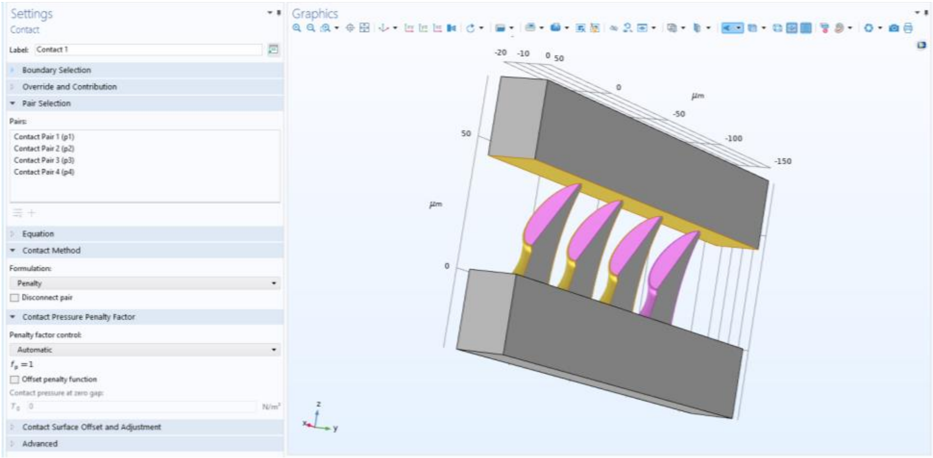

Settings
Contact
Label: Contact 1
Boundary Selection
Override and Contribution
Pair Selection
Pairs:
Contact Pair 1 (p1)
Contact Pair 2 (p2)
Contact Pair 3 (p3)
Contact Pair 4 (p4)
Equation
Contact Method
Formulation:
Penalty
☐ Disconnect pair
Contact Pressure Penalty Factor
Penalty factor control:
Automatic
$f_p = 1$
☐ Offset penalty function
Contact pressure at zero gap:
T_0 0 N/m²
Contact Surface Offset and Adjustment
Advanced

Figure 3.23 Contact pairs of MS in COMSOL.

Hyperelastic Material was assigned to half setae and the lower block. The parameters of the fifth-order Mooney-Rivlin were -1.81 MPa, 3.14 MPa, 9.82e-12 MPa, -0.152 MPa and 0.683 MPa, corresponding to C_{10}, C_{01}, C_{20}, C_{02}, and C_{11}, respectively [44]. In addition, the fixed constraint and symmetry were applied to the geometry, as Figure 3.24 shows. Lastly, Prescribed Displacement was assigned to the upper block, which would move downward from 0 to 23 µm with a 0.05 µm increment.

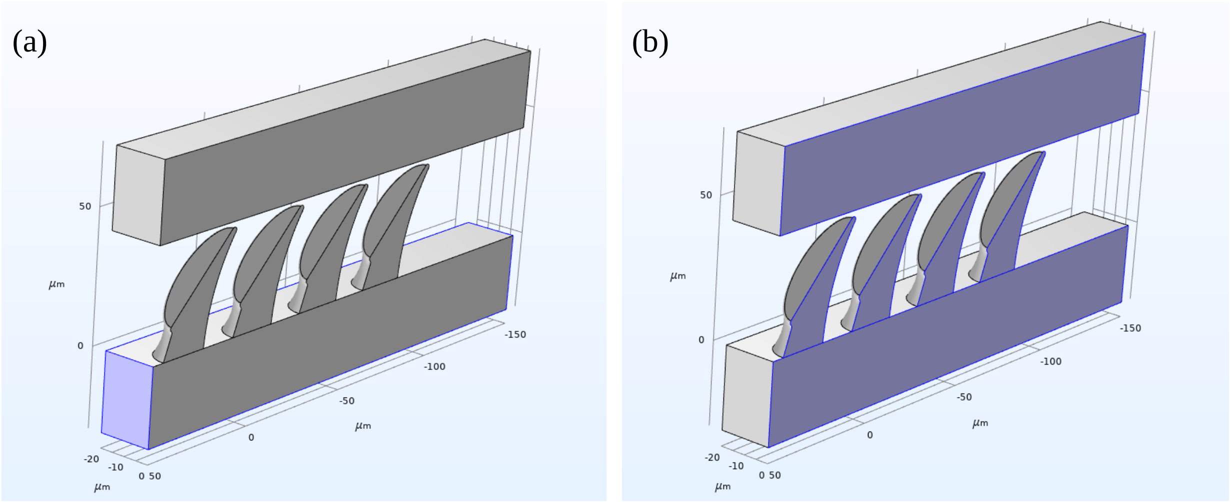

Figure 3.24 (a) Fixed constraint on the lower block. (b) Symmetry on the geometry.

The aluminum plate was 3 µm above the miniature microstructures and would move straight down for 23 µm to compress the miniature microstructures. The Von Mises stresses of compressed designs of miniature microstructures are shown in Figure 3.25. The pillars of the tilted mushroom-shaped designs experienced higher compression stress than the wedge-shaped design. The maximum compression stresses of the mushroom-shaped designs were located at the bottom right corner of the pillars, as Figure 3.25 (a) and (b) show. For the wedge-shaped designs, the higher stress was found in the middle of the tilted panel and the bottom right corner of the wedge-shaped design, as Figure 3.25 (c) and (d) shown. The higher stress on the tilted panel of the WS design would cause the structural fracture, which matched the experimental result shown in Figure 3.19 (b).

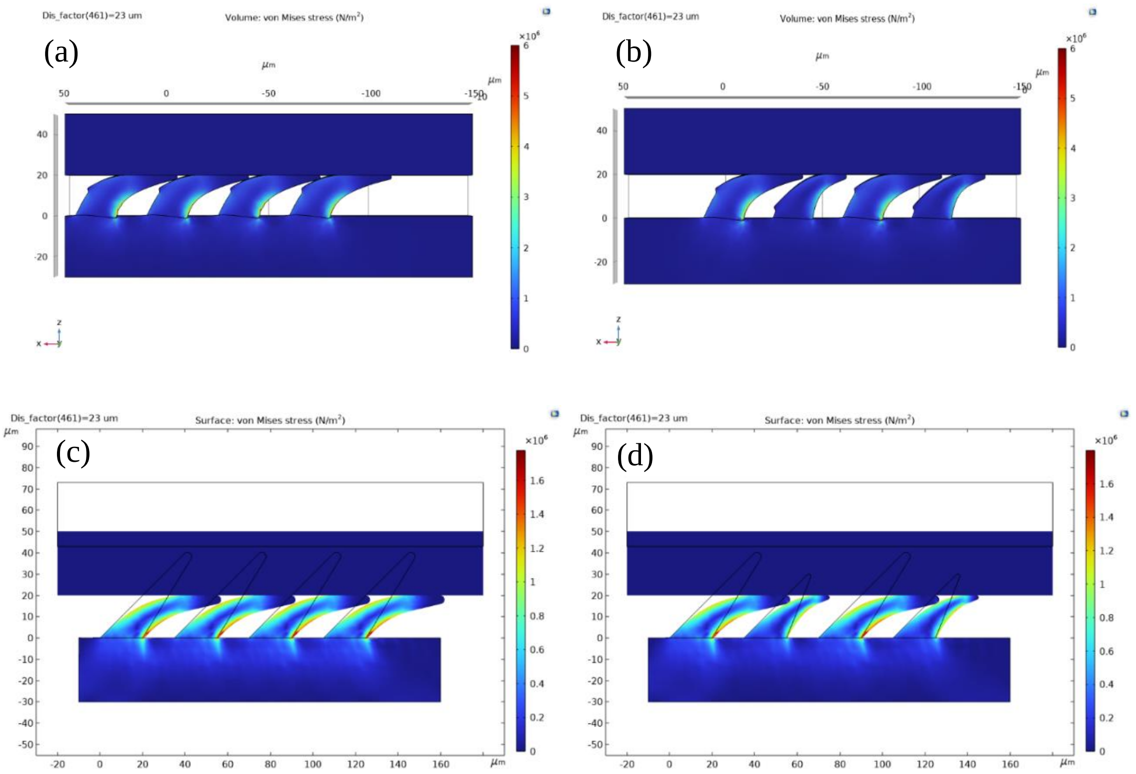

Figure 3.25 Von Mises stresses of compressed miniature microstructures in COMSOL. (a) MS design (b) MD design (c) WS design (d) WD design.

The contact areas of the miniature microstructures were obtained by calculating the intersection of the miniature microstructures and the aluminum plate; then, the values would be multiplied by the number of a set of four artificial setae in 1 cm^2, which was 23,565 sets. The calculated contact areas were normalized by dividing the 1 cm^2 to estimate the ratio of the effective contact area to the total area, and the results are shown in Figure 3.26. As the miniature microstructures were compressed, wedge-shaped designs would eventually have a higher effective contact area than the mushroom-shaped design on a plat plane.

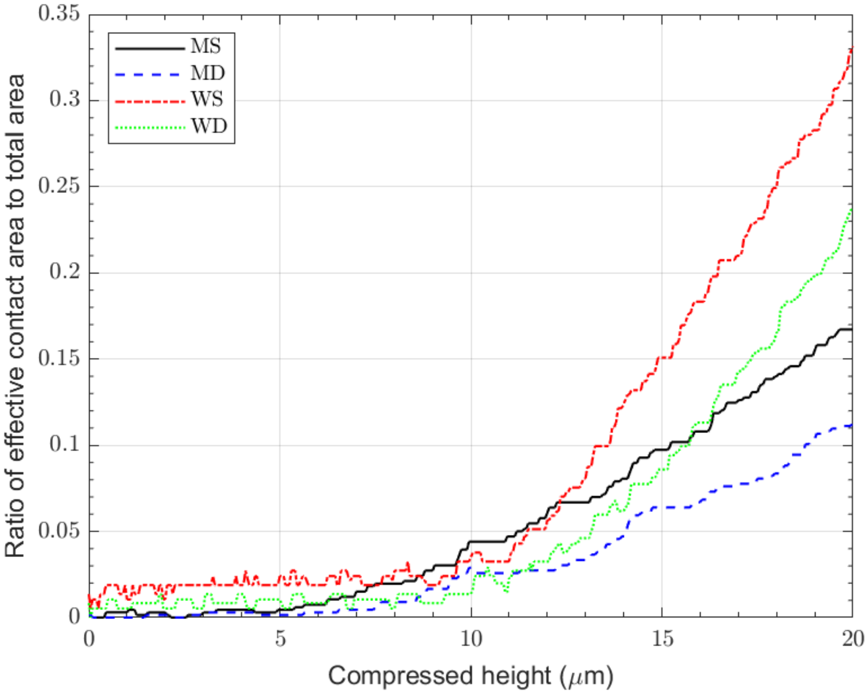

Figure 3.26 Ratio of effective contact area to total area during the compression.

4 Conclusion

In this thesis, an advanced and cost-effective fabrication process was developed to produce a simplified gecko-inspired microstructure with 2PP and polymer molding. After the master molds were printed with 2PP 3D printing process and were spin-coated with 5% PAA, they were cast with PDMS to produce negative molds. The negative molds would be produced once the PDMS was degassed and cured at 40°C for 12 hours. Similarly, the replicated positive molds would be obtained with the same molding process by casting PDMS onto the demolded PDMS negative molds. The presented microstructures fabrication process could produce micropillar with a height of 270 μm without any defect. However, this fabrication process was unsuitable for producing the micropillar with a height of fewer than 40 μm because the problems of missing and damaged microstructures existed. The PDMS positive molds fabricated with this process must be cleaned with DI water to remove the PAA isolated layer, inhibiting the adhesion between PDMS and the attached surfaces.

The adhesion performances of the pure PDMS flat plane and micro structured PDMS were related to the applied preload force. The maximum adhesions tended to increase and remain stable as the preload force increased. Although the adhesion performance of the micro structured PDMS is lower than the pure PDMS flat plane, those microstructures provided outstanding controllability in adhesion by shearing the microstructures. The maximum adhesions of the gecko-inspired microstructures varied on different surfaces, but the cause of the variation was not investigated. However, the experiment showed that the maximum adhesions did not directly correlate to the surface roughness and surface energy.

The experiments showed that the adhesion of the microstructures with alternating heights of artificial setae was higher than those with uniform height as the applied preload force increased.

However, as the positive molds were sheared, the adhesion of the microstructures with constant height was far more than the adhesion of designs with different heights of micropillar. Meanwhile, the effects of the scale and the shape of the artificial gecko setae were discovered. The miniature microstructures, which had a height of 40 μm, had lower adhesion than the microstructures with a height of 270 μm. The damaged miniature microstructures might cause the cause of the reduced adhesion on the PDMS positive molds. Furthermore, the wedge-shaped designs had better adhesive performance than the mushroom-shaped designs due to their structural advantage of low bending resistance when preload force was applied, and the effective contact area of the wedge-shaped designs was larger than the mushroom-shaped designs.

5 Future Work

The microstructure fabrication process still needs to be improved to produce the micropillar with a height of 40 μm or less. The factors that caused the damaged micropillar on the PDMS positive mold might be the non-fully covered isolated layer and manually demolding. The sample could be treated to have a more hydrophilic surface with some chemicals and techniques to help 5% PAA spread on the microstructure and fully cover the microstructure when it dries out to form an isolated layer. The demolding process could be improved by having a machine pull the cured molds at a low and controllable speed. The designs of the micropillar in this work were conservative to ensure the feasibility of fabricating artificial gecko setae without defects. The limitation of the presented fabrication process will be investigated by producing the micropillar with a higher aspect ratio, smaller size, and more complicated shapes.

REFERENCE

[1] "Space Environment Statistics." Vol. 2022, ESA's Space Debris Office, 2022.

[2] Sánchez, A. H., Soares, T., and Wolahan, A. "Reliability aspects of mega-constellation satellites and their impact on the space debris environment," *2017 Annual Reliability and Maintainability Symposium (RAMS)*. 2017, pp. 1-5. https://doi.org/10.1109/RAM.2017.7889671

[3] Mark, C. P., and Kamath, S. "Review of active space debris removal methods," *Space Policy* Vol. 47, 2019, pp. 194-206. https://doi.org/10.1016/j.spacepol.2018.12.005

[4] Soulard, R., Quinn, M. N., Tajima, T., and Mourou, G. "ICAN: A novel laser architecture for space debris removal," *Acta Astronautica* Vol. 105, No. 1, 2014, pp. 192-200. https://doi.org/10.1016/j.actaastro.2014.09.004

[5] Bombardelli, C., and Pelaez, J. "Ion beam shepherd for contactless space debris removal," *Journal of guidance, control, and dynamics* Vol. 34, No. 3, 2011, pp. 916-920. https://doi.org/10.2514/1.51832

[6] Kawamoto, S., Ohkawa, Y., Kitamura, S., and Nishida, S.-i. "Strategy for active debris removal using electrodynamic tether," *Transactions of the Japan Society for Aeronautical and Space Sciences, Space Technology Japan* Vol. 7, No. ists26, 2009, pp. Pr_2_7-Pr_2_12. https://doi.org/10.2322/tstj.7.Pr_2_7

[7] Muller, P. "Glossary of terms used in physical organic chemistry (IUPAC Recommendations 1994)," *Pure and Applied Chemistry* Vol. 66, No. 5, 1994, pp. 1077-1184. https://doi.org/10.1351/pac199466051077

[8] Gillies, A. G., Henry, A., Lin, H., Ren, A., Shiuan, K., Fearing, R. S., and Full, R. J. "Gecko toe and lamellar shear adhesion on macroscopic, engineered rough surfaces," *Journal of Experimental Biology* Vol. 217, No. 2, 2014, pp. 283-289. https://doi.org/10.1242/jeb.092015

[9] Ruibal, R., and Ernst, V. "The structure of the digital setae of lizards," *Journal of Morphology* Vol. 117, No. 3, 1965, pp. 271-293. https://doi.org/10.1002/jmor.1051170302

[10] Li, Y., Krahn, J., and Menon, C. "Bioinspired Dry Adhesive Materials and Their Application in Robotics: A Review," *Journal of Bionic Engineering* Vol. 13, No. 2, 2016, pp. 181-199. https://doi.org/10.1016/S1672-6529(16)60293-7

[11] Bhushan, B. "Adhesion of multi-level hierarchical attachment systems in gecko feet," *Journal of Adhesion Science and Technology* Vol. 21, No. 12-13, 2007, pp. 1213-1258.

https://doi.org/10.1163/156856107782328353

[12] Israelachvili, J. N. *Intermolecular and surface forces*: Academic press, 2011.

[13] Wang, Z. "Slanted Functional Gradient Micropillars for Optimal Bioinspired Dry Adhesion," *ACS Nano* Vol. 12, No. 2, 2018, pp. 1273-1284.
https://doi.org/10.1021/acsnano.7b07493

[14] Castellanos, G., Arzt, E., and Kamperman, M. "Effect of Viscoelasticity on Adhesion of Bioinspired Micropatterned Epoxy Surfaces," *Langmuir* Vol. 27, No. 12, 2011, pp. 7752-7759.
https://doi.org/10.1021/la2009336

[15] Davies, J., Haq, S., Hawke, T., and Sargent, J. P. "A practical approach to the development of a synthetic Gecko tape," *International Journal of Adhesion and Adhesives* Vol. 29, No. 4, 2009, pp. 380-390.
https://doi.org/10.1016/j.ijadhadh.2008.07.009

[16] Liu, Q., Tan, D., Meng, F., Yang, B., Shi, Z., Wang, X., Li, Q., Nie, C., Liu, S., and Xue, L. "Adhesion Enhancement of Micropillar Array by Combining the Adhesive Design from Gecko and Tree Frog," *Small* Vol. 17, No. 4, 2021, p. 2005493.
https://doi.org/10.1002/smll.202005493

[17] Chu, Z., Wang, C., Hai, X., Deng, J., Cui, J., and Sun, L. "Analysis and Measurement of Adhesive Behavior for Gecko-Inspired Synthetic Microwedge Structure," *Advanced Materials Interfaces* Vol. 6, No. 12, 2019, p. 1900283.
https://doi.org/10.1002/admi.201900283

[18] Seo, J., Eisenhaure, J., and Kim, S. "Micro-wedge array surface of a shape memory polymer as a reversible dry adhesive," *Extreme Mechanics Letters* Vol. 9, 2016, pp. 207-214.
https://doi.org/10.1016/j.eml.2016.07.007

[19] Murphy, M. P., Aksak, B., and Sitti, M. "Gecko-Inspired Directional and Controllable Adhesion," *Small* Vol. 5, No. 2, 2009, pp. 170-175.
https://doi.org/10.1002/smll.200801161

[20] Wang, Y., Li, X., Tian, H., Hu, H., Tian, Y., Shao, J., and Ding, Y. "Rectangle-capped and tilted micropillar array for enhanced anisotropic anti-shearing in biomimetic adhesion," *Journal of The Royal Society Interface* Vol. 12, No. 106, 2015, p. 20150090.
https://doi.org/10.1098/rsif.2015.0090

[21] Parness, A., Soto, D., Esparza, N., Gravish, N., Wilkinson, M., Autumn, K., and Cutkosky, M. "A microfabricated wedge-shaped adhesive array displaying gecko-like dynamic adhesion, directionality and long lifetime," *Journal of The Royal Society Interface* Vol. 6, No. 41, 2009, pp. 1223-1232.
https://doi.org/10.1098/rsif.2009.0048

[22] Aksak, B., Murphy, M. P., and Sitti, M. "Adhesion of Biologically Inspired Vertical and Angled Polymer Microfiber Arrays," *Langmuir* Vol. 23, No. 6, 2007, pp. 3322-3332. https://doi.org/10.1021/la062697t

[23] Hu, H., Tian, H., Shao, J., Wang, Y., Li, X., Tian, Y., Ding, Y., and Lu, B. "Friction Contribution to Bioinspired Mushroom-Shaped Dry Adhesives," *Advanced Materials Interfaces* Vol. 4, No. 9, 2017, p. 1700016. https://doi.org/10.1002/admi.201700016

[24] Hu, H., Tian, H., Li, X., Shao, J., Ding, Y., Liu, H., and An, N. "Biomimetic Mushroom-Shaped Microfibers for Dry Adhesives by Electrically Induced Polymer Deformation," *ACS Applied Materials & Interfaces* Vol. 6, No. 16, 2014, pp. 14167-14173. https://doi.org/10.1021/am503493u

[25] Yi, H., Kang, M., Kwak, M. K., and Jeong, H. E. "Simple and Reliable Fabrication of Bioinspired Mushroom-Shaped Micropillars with Precisely Controlled Tip Geometries," *ACS Applied Materials & Interfaces* Vol. 8, No. 34, 2016, pp. 22671-22678. 10.1021/acsami.6b07337

[26] Krahn, J., Sameoto, D., and Menon, C. "Controllable biomimetic adhesion using embedded phase change material," *Smart Materials and Structures* Vol. 20, No. 1, 2010, p. 015014. https://doi.org/10.1088/0964-1726/20/1/015014

[27] Lee, S. H., Kim, S. W., Kang, B. S., Chang, P.-S., and Kwak, M. K. "Scalable and continuous fabrication of bio-inspired dry adhesives with a thermosetting polymer," *Soft Matter* Vol. 14, No. 14, 2018, pp. 2586-2593. https://doi.org/10.1039/C7SM02354E

[28] Li, X., Tao, D., Lu, H., Bai, P., Liu, Z., Ma, L., Meng, Y., and Tian, Y. "Recent developments in gecko-inspired dry adhesive surfaces from fabrication to application," *Surface Topography: Metrology and Properties* Vol. 7, No. 2, 2019, p. 023001. https://doi.org/10.1088/2051-672X/ab1447

[29] Murphy, M. P., Aksak, B., and Sitti, M. "Adhesion and anisotropic friction enhancements of angled heterogeneous micro-fiber arrays with spherical and spatula tips," *Journal of Adhesion Science and Technology* Vol. 21, No. 12-13, 2007, pp. 1281-1296. https://doi.org/10.1163/156856107782328380

[30] Busche, J. F., Starke, G., Knickmeier, S., and Dietzel, A. "Controllable dry adhesion based on two-photon polymerization and replication molding for space debris removal," *Micro and Nano Engineering* Vol. 7, 2020, p. 100052. https://doi.org/10.1016/j.mne.2020.100052

[31] Santos, D., Spenko, M., Parness, A., Kim, S., and Cutkosky, M. "Directional adhesion for climbing: theoretical and practical considerations," *Journal of Adhesion Science and Technology* Vol. 21, No. 12-13, 2007, pp. 1317-1341. https://doi.org/10.1163/156856107782328399

[32] Day, P., Eason, E. V., Esparza, N., Christensen, D., and Cutkosky, M. "Microwedge Machining for the Manufacture of Directional Dry Adhesives," *Journal of Micro and Nano-Manufacturing* Vol. 1, No. 1, 2013.
https://doi.org/10.1115/1.4023161

[33] Chary, S., Tamelier, J., and Turner, K. "A microfabricated gecko-inspired controllable and reusable dry adhesive," *Smart materials and structures* Vol. 22, No. 2, 2013, p. 025013.
https://doi.org/10.1088/0964-1726/22/2/025013

[34] Tao, D., Gao, X., Lu, H., Liu, Z., Li, Y., Tong, H., Pesika, N., Meng, Y., and Tian, Y. "Controllable Anisotropic Dry Adhesion in Vacuum: Gecko Inspired Wedged Surface Fabricated with Ultraprecision Diamond Cutting," *Advanced Functional Materials* Vol. 27, No. 22, 2017, p. 1606576.
https://doi.org/10.1002/adfm.201606576

[35] Autumn, K., and Puthoff, J. "Properties, principles, and parameters of the gecko adhesive system," *Biological adhesives*. Springer, 2016, pp. 245-280.

[36] Heepe, L., Xue, L., and Gorb, S. N. *Bio-inspired structured adhesives: biological prototypes, fabrication, tribological properties, contact mechanics, and novel concepts*: Springer, 2017.

[37] Wu, X., Wang, X., Mei, T., and Sun, S. "Mechanical analyses on the digital behaviour of the Tokay gecko (Gekko gecko) based on a multi-level directional adhesion model," *Proceedings. Mathematical, physical, and engineering sciences* Vol. 471, No. 2179, 2015, pp. 20150085-20150085.
https://doi.org/10.1098/rspa.2015.0085

[38] Autumn, K., Majidi, C., Groff, R. E., Dittmore, A., and Fearing, R. "Effective elastic modulus of isolated gecko setal arrays," *Journal of Experimental Biology* Vol. 209, No. 18, 2006, pp. 3558-3568.
https://doi.org/10.1242/jeb.02469

[39] Hensel, R., Moh, K., and Arzt, E. "Engineering Micropatterned Dry Adhesives: From Contact Theory to Handling Applications," *Advanced Functional Materials* Vol. 28, No. 28, 2018, p. 1800865.
https://doi.org/10.1002/adfm.201800865

[40] Lamblet, M., Verneuil, E., Vilmin, T., Buguin, A., Silberzan, P., and Léger, L. "Adhesion Enhancement through Micropatterning at Polydimethylsiloxane−Acrylic Adhesive Interfaces," *Langmuir* Vol. 23, No. 13, 2007, pp. 6966-6974.
https://doi.org/10.1021/la063104h

[41] Gillies, A. G., Kwak, J., and Fearing, R. S. "Controllable Particle Adhesion with a Magnetically Actuated Synthetic Gecko Adhesive," *Advanced Functional Materials* Vol. 23, No. 26, 2013, pp. 3256-3261.
https://doi.org/10.1002/adfm.201203122

[42] Wang, Y., Tian, H., Shao, J., Sameoto, D., Li, X., Wang, L., Hu, H., Ding, Y., and Lu, B. "Switchable Dry Adhesion with Step-like Micropillars and Controllable Interfacial Contact," *ACS Applied Materials & Interfaces* Vol. 8, No. 15, 2016, pp. 10029-10037. https://doi.org/10.1021/acsami.6b01434

[43] Wu, S., Serbin, J., and Gu, M. "Two-photon polymerisation for three-dimensional micro-fabrication," *Journal of Photochemistry and Photobiology A: Chemistry* Vol. 181, No. 1, 2006, pp. 1-11. https://doi.org/10.1088/0964-1726/22/2/025013

[44] Son, D., Liimatainen, V., and Sitti, M. "Machine Learning-Based and Experimentally Validated Optimal Adhesive Fibril Designs," *Small* Vol. 17, No. 39, 2021, p. 2102867. https://doi.org/10.1002/smll.202102867

[45] Nanoscribe. "Removal and Stripping." Vol. 2022.

[46] Corporation, D. C. "SYLGARD® 184 Silicone Elastomer Product Information."

[47] Chuang, T.-K., Usenko, A., and Cites, J. "Bonding Energy of Silicon-to-Glass Wafer Bonding," *ECS Meeting Abstracts*. IOP Publishing, 2010, p. 1713. https://doi.org/10.1149/MA2010-02/27/1713

[48] Kroner, E., Paretkar, D. R., McMeeking, R. M., and Arzt, E. "Adhesion of Flat and Structured PDMS Samples to Spherical and Flat Probes: A Comparative Study," *The Journal of Adhesion* Vol. 87, No. 5, 2011, pp. 447-465. https://doi.org/10.1080/00218464.2011.575317

[49] Liang, C., Wang, F., Huo, Z., Shi, B., Tian, Y., Zhao, X., and Zhang, D. "Pull-off force modeling and experimental study of PDMS stamp considering preload in micro transfer printing," *International Journal of Solids and Structures* Vol. 193-194, 2020, pp. 134-140. https://doi.org/10.1016/j.ijsolstr.2020.02.011